AEROSOL-CLOUD INTERACTIONS FROM HAWAII'S KĪLAUEA VOLCANO

A THESIS SUBMITTED TO THE GRADUATE DIVISION OF THE UNIVERSITY OF HAWAI'I AT MĀNOA IN PARTIAL FULFILLMENT OF THE REQUIREMENTS FOR THE DEGREE OF

MASTER OF SCIENCE

IN

ATMOSPHERIC SCIENCES

AUGUST 2018

By

Kayla K. Yamamoto

Thesis Committee:
Jennifer D. Small Griswold, Chairperson
Alison D. Nugent
Steven Businger

Keywords: Aerosol indirect effects, sulfate aerosols, volcanic emissions, vog

ACKNOWLEDGEMENTS

I would like to thank the collaborators of the Vog Measurement and Prediction (VMAP) project for providing the Vog model data that helped define the uniqueness of this study. Living in Hawaii, I experience firsthand how vog pollution can have negative impacts on local communities, and thus greatly appreciate the extensive efforts being made to address this issue. I would also like to extend an additional thanks to Lacey Holland and Andre Pattantyus for taking the time out of their busy schedules to supply the archived VMAP data sets that were used in this study. I would like to express my deepest gratitude to my advisor, Jennifer Griswold, for her invaluable guidance and support that was essential in my growth not only as a researcher, but as a person in my years as her student. Her passion for science and gift for teaching is what initially convinced me to embark down this journey as a student in atmospheric sciences, and I am forever grateful for the incredible impact she has made on my life. I would also like to thank my thesis committee, Steven Businger and Alison Nugent, for their input and constructive criticism that was instrumental in shaping and furthering this study. Lastly, I would like to express my appreciation to my family and friends for their love and support throughout the years. A special thanks to my parents for always encouraging me to follow my dreams, and to Sean, Mariah, Ashley, and Jessie for making this experience and unforgettable one. I truly appreciate you all.

ABSTRACT

Aerosols, clouds, and their interactions play significant roles in both the Earth's radiative budget and hydrological cycle. Therefore, it is necessary to establish meaningful relationships between aerosols, clouds, and climate in order to improve our understanding of global climate change. However, due to the complex feedbacks involved, aerosol-cloud interactions (ACI) remain poorly understood and account for much of the current uncertainty in global climate models. Kīlauea volcano on the Big Island of Hawaii provides a unique opportunity to study ACI in a setting where sulfur is continuously emitted into a clean marine boundary layer. This natural laboratory allows for a simplified analysis of ACI in warm trade wind cumulus downwind of Kīlauea volcano. Furthermore, we address the complication of orographic effects in investigating changes in cloud properties downwind of the Hawaiian Islands. This is an important distinction from previous Hawaii studies, which have attributed changes in cloud properties to either ACI or orographic effects. Instead, we propose a combined ACI and orographic effect and include both within our analysis.

In this study, we combine Level-2 Collection 6 cloud properties from the MODerate-Resolution Imaging Spectroradiometer (MODIS) aboard the Aqua platform, together with Vog model results from the Vog Measurement and Prediction (VMAP) project to compare clouds within the Kīlauea aerosol plume to nearby clouds located out of the aerosol plume (both pristine and orographic). From the 127 MODIS cases selected during the months of June, July, and August from 2011 – 2017, we found clouds located within the Kīlauea aerosol plume to have smaller droplets, increased thickness, increased liquid water content, higher cloud tops, and increased fractional coverage compared to out of plume clouds. These findings agree with previous Kīlauea studies and provide evidence for the first and second indirect effects.

TABLE OF CONTENTS

LIST OF TABLES

LIST OF FIGURES

CHAPTER 1
INTRODUCTION

1.1 Aerosols and Climate

Aerosols are tiny airborne particles of liquid and/or solid mass that are suspended in the atmosphere. They originate from both natural and anthropogenic sources, and are emitted directly into their environment as primary aerosols, or form through gas-to-particle conversion as secondary particles. In the troposphere, aerosols experience a lifetime of about a week before being removed via sedimentation, rainout, and runoff processes (Myhre et al. 2013). During this relatively short existence, they undergo complex interactions with clouds and solar radiation, and therefore are intricately linked to the hydrological cycle and global energy balance. This occurs directly through the scattering and absorption of incoming solar radiation (McCormick and Ludwig 1967), and indirectly by altering the distribution and radiative properties of clouds (Twomey 1977; Albrecht 1989; Pincus and Baker 1994). Unlike greenhouse gases (GHGs), which trap outgoing longwave radiation and warm the planet, aerosols have an overall cooling effect, which has masked the estimated anthropogenic GHG forcing of 2.3 W m^{-2} during the industrial era with a radiative forcing of -0.9 W m^{-2} (Myhre et al. 2013; Boucher et al. 2013). Due to this global cooling potential, aerosols have become a major focus in climate research and geoengineering considerations.

1.1.1 Volcanic Aerosols

Volcanoes provide an excellent natural source of sulfur dioxide (SO_2), a toxic colorless gas that can cause irritation to the eyes, mouth, and lungs, along with respiratory distress due to increased exposure. In the atmosphere, SO_2 undergoes various chemical reactions in order to convert to sulfate (SO_4) aerosol, including the oxidation of SO_2 to SO_4, the mixing of SO_2 with water vapor to form sulfuric acid

(H_2SO_4), and the nucleation or condensation of SO_2 onto existing SO_4 aerosols. The resulting sulfur particles are highly acidic and are a primary component of acid rain, which can lead to property, agricultural, and environmental damages to the affected communities and ecosystems.

Particulate sulfate is especially hazardous due to its exceedingly small size characterized by a diameter of 2.5 microns or less ($PM_{2.5}$), allowing particles to travel deeper into the respiratory track and lungs for more severe and, in some cases, fatal health complications. Overall, studies have found higher $PM_{2.5}$ concentrations to be highly correlated with increased mortality (Dockery et al. 1993). In addition, $PM_{2.5}$ is highly efficient at scattering radiation, and because these fine particulates are smaller in mass, can linger and accumulate more effectively in the atmospheric boundary layer. Using Mie theory, Lacis (2015) showed that mature volcanic aerosols have a typical particle size that falls within the range of peak scattering efficiency for non-absorbing aerosols. Thus, we can see why optical phenomena—including milky white skies, red sunsets, dust veils, and volcanic aerosol clouds—have been observed following past volcanic eruptions, and why at high concentrations these particles diminish visibility and may present a hazard to aviation. Furthermore, this scattering ability affects the global climate system by increasing the planetary albedo and decreasing the amount of incoming solar radiation that reaches Earth's surface (Robock 2000). The net result is a volcanically induced surface cooling that is often noted following large volcanic eruptions, such as the infamous Mount St. Helens eruption of 1980 or Mount Pinatubo in 1991. During these types of events, substantial amounts of sulfur are injected into the lower stratosphere, where aerosols experience a significantly longer lifetime on the order of a year (Robock 2000). Other conditions, such as stratospheric winds, favor the formation and planetary scale transport of aerosols around the globe, allowing volcanic radiative effects to become increasingly pronounced. In addition to this, stratospheric eruptions have been linked to other atmospheric changes involving differential heating patterns, circulation modes, and

ozone depletion (Robock 2000; Forster et al. 2007; Meyer et al. 2016; Smith et al. 2016). For more information on the climatic impacts of large volcanic eruptions refer to Robock (2000).

1.2 Clouds and Climate

Clouds are made up of liquid droplets and ice crystals that are tiny enough to remain aloft, yet big enough to create a visible aggregate. They form when air containing moisture rises, expands, and cools to the point of condensation, commonly referred to as the dew point temperature. In the atmosphere, this occurs via a lifting mechanism, such as the lifting along an orographic or frontal barrier, turbulence, or surface heating and convection (Ahrens 2012). Depending on their micro- and macrophysical properties, clouds may reflect incoming solar radiation to cool the surface, trap outgoing longwave radiation to warm the surface, or be characterized by a combination of both. This radiative effect is climatically significant since clouds cover more than half of the Earth at any given time.

Throughout a cloud's lifetime, a myriad of environmental factors affect whether clouds precipitate, evaporate, or continue to develop. During cloud formation, latent heat energy is released into the environment through the condensation of water vapor to form liquid cloud droplets, the freezing of super-cooled droplets to form ice crystals, and through vapor deposition. Cloud particles may grow, via the collision and coalescence of liquid droplets or through the Wegener-Bergeron-Findeisen process for ice crystals, and become substantial enough to fall to the surface as precipitation. They may also evaporate or melt under certain conditions, taking heat energy from the environment. In some cases, strong cloud updrafts may loft hydrometeors above the freezing level, allowing the aggregation of cloud ice and water to form hail. These types of storm clouds are also associated with heavy rain, flooding, lightning, and in extreme cases, tornadoes. Altogether, we see that clouds play a significant role in the Earth-atmosphere system via the global redistribution of water and energy.

1.2.1 Shallow Marine Clouds

In particular, shallow marine clouds, which cover much of the tropical and subtropical oceans, are climatically important. This is because they reflect incoming solar radiation with little to no effect on outgoing longwave radiation, allowing them to perturb the global energy budget beyond that of any other cloud type (Hartmann and Doelling 1980; Hartmann et al. 1992; Pincus and Baker 1994; Stevens and Feingold 2009; Wood 2012; Liu et al. 2015). Additionally, these low-level clouds are important in determining the energetics and structure of the marine boundary layer (MBL) through its role in ocean-atmosphere fluxes. The importance of shallow marine clouds in global moisture and energy budgets has long been noted and thus has fueled efforts in investigating these types of clouds as early as 1923, when the first research aircraft flight studied marine stratocumulus cloud decks off the coast of California (Kloesel 1992). Over time, improvements in satellite technology have allowed shallow marine clouds to be further explored, yet these studies continue to focus on marine stratocumuli due to their increased cloud cover. On the other hand, trade wind cumuli (TCu) remain under-investigated (Norris and Slingo 2009). The issue is that TCu tend to be significantly smaller, broken, and inhomogeneous in their spatial and temporal extent, compared to other shallow marine cloud regimes (Werner et al. 2014). This requires high-resolution satellite data to study TCu that is not always available. For this reason, our study focuses on shallow marine clouds with a specific interest in the TCu cloud regime.

TCu clouds, also referred to as fair-weather cumulus or *cumulus humilis*, are boundary layer cumuli that have cloud bases around an altitude of 2,000 – 2,500 feet, and only grow to be about 5,000 – 7,000 feet thick due to a capping inversion limiting their vertical growth (AMS glossary). TCu tend to form due to the breakup of a well-mixed stratus or stratocumulus layer, which forms off the west coasts of major continents due to a semi-permanent subtropical high-pressure system that promotes the upwelling of deep ocean water, cooling the air near the surface and stabilizing the lower troposphere. The eastern portion of the high-pressure system

brings air equatorward with sea surface temperatures (SSTs) increasing towards the equator. During this process, convective eddies intensify and increase entrainment into the inversion layer, leading to the decoupling of the well-mixed stratus layer from the newly formed stable boundary layer that exists below cloud base (Cotton et al. 2010). As the air continues equatorward, the increasing SSTs continue to invigorate the convective eddies, which in turn increases cumulus entrainment of dry inversion air, and leads to the dissipation of the stratocumulus layer due to evaporation. Near the equator, the large-scale subsidence becomes nearly zero, increasing the depth of the MBL (Neiburger et al. 1961; Schubert et al. 1979; Klein and Hartman 1993). Through this process, there is a transition that occurs from a well-mixed stratus layer, to a decoupled region of cumulus-under-stratus, to a dissipating stratocumulus layer, and finally to the TCu cloud regime (Klein et al. 1995).

1.3 Aerosol-Cloud Interactions (ACI)

Understanding the link between aerosols and clouds has been noted as early as the 1900's, when anomalous 'ship tracks' in marine stratus cloud structures were increasingly being noted in ship and aviation observations (Russell et al. 1999). What may have seemed like a straightforward relationship between aerosol and clouds, has proved to be one of the biggest problems in understanding past, present, and future climate change. Over the past two decades, improvements in satellite technology have allowed researchers to examine aerosol-cloud interactions (ACI) on improved spatial and temporal scales. However, studies have found it exceedingly difficult to establish quantitatively meaningful relationships between aerosols, clouds, and climate. This is largely due to the numerous and complex feedback systems involved in ACI that often result in alternate explanations, such as co-varying meteorology or retrieval artifacts, for observed correlations between aerosol loading and changes in cloud properties (Kaufman et al. 2002; Stevens and Feingold 2009; Koren et al. 2010; Yuan et al. 2011). In addition, both aerosol and cloud

properties vary extensively over time and space, adding to the already difficult task of unraveling ACI feedbacks (Kaufman et al. 2002). As a result, the role of ACI in global climate forcing models remains highly uncertain (Quaas et al. 2009; Boucher et al. 2013).

It is well-known that aerosols are an essential ingredient in cloud formation. In a pristine atmosphere, the formation of pure liquid cloud droplets would entail water vapor molecules to collide spontaneously through the process of homogenous nucleation. The survival of such droplets would require extremely high supersaturation levels not readily observed in nature due to surface tension effects inhibiting cloud droplet growth (Rogers and Yau 1989). Fortunately, aerosols can serve as cloud condensation nuclei (CCN), providing the necessary activation sites for cloud formation through heterogeneous nucleation. Furthermore, through these interactions, aerosols are able to modify the physical and radiative properties of clouds.

1.3.1 First Indirect Effect

If we imagine a cloud that forms in a clean environment, such as a maritime air mass, we would expect the cloud to be composed of large cloud droplets since there would be fewer aerosol particles available to act as CCN. In contrast, if the cloud instead forms in a polluted environment, such as a continental air mass, the same liquid water amount would be divided up among more CCN, resulting in smaller and more numerous cloud droplets, providing more surface area to reflect radiation so that the cloud appears brighter (Figure 1.1a). This is called the first indirect effect, also referred to as the cloud albedo effect or Twomey effect. It occurs in warm clouds when an increase in aerosol load results in more numerous small cloud droplets, and an overall more reflective cloud (Twomey 1977). Werner et al. (2014) looked at shallow marine clouds near Barbados using collocated microphysical and remote sensing measurements and showed that there were smaller cloud droplets, optically thicker clouds, and more reflective cloud properties associated with

increased aerosol load, providing evidence for the first indirect effect in the trade wind regime.

1.3.2 Second Indirect Effect

A subsequent process follows the first indirect effect in which the smaller cloud droplets, which are less efficient at collision and coalescence, take longer to form raindrops and thus lead to suppressed precipitation, higher cloud tops, longer-lived clouds, and an overall increased cloud amount (Pincus and Baker 1994; Albrecht 1989). This is called the second indirect effect, also referred to as the cloud lifetime effect or Albrecht effect, and is summarized in Figure 1.1b. For a detailed review on aerosol indirect effects—including the semi-direct effect, surface energy budget effect, and indirect effects for mixed-phase clouds not covered in this thesis—refer to Lohmann and Feichter (2005).

1.3.3 An Approach to ACI

The idea of modifying weather and climate by introducing particles into clouds has sparked interest as early as the 1940's, with the idea of 'cloud seeding.' Rather than increased aerosol concentration leading to suppressed precipitation and increased cloud amount, as proposed by the first and second indirect effects for warm clouds, cloud seeding suggests that the addition of certain particles, such as silver iodide or salt, into super-cooled clouds would lead to the rapid formation of ice crystals, increasing the likelihood of precipitation. This demonstrates the critical importance that different types of aerosols and clouds may have in producing completely different ACI responses, thus stressing the importance of using an approach to ACI that is both cloud regime and region specific (Stevens and Feingold 2009). Because TCu exist well below the freezing level and within a clean MBL, they are classified as warm clouds and are highly sensitive to changes in aerosol loading, as in the case of man-made ship tracks. Thus, TCu are a suitable candidate to study ACI.

1.4 Volcanic ACI

Studies have shown the effectiveness of using natural laboratories, such as effusive volcanoes, to investigate the impacts of sulfur aerosols on clouds and climate. Unlike explosive volcanic eruptions, which have been heavily studied due to their capability for stratospheric aerosol injection (Robock 2000), effusive volcanoes have only recently gained attention in the climate research community. These volcanoes differ in that they release volcanic aerosols into the lower troposphere and have generally weaker but continuous volcanic activity, therefore providing valuable opportunities to investigate the effects of volcanic aerosols on downstream cloud properties.

Schmidt et al. (2012) used a global aerosol microphysics model to determine the importance of continuously degassing volcanoes for the indirect radiative forcing of climate. Tropospheric volcanic aerosols were found to be a substantial source of global CCN, increasing the global mean cloud droplet number concentration (CDNC) by about 10%. They were also shown to significantly modify the microphysical properties of low- and mid-level clouds. Moreover, by comparing volcanic aerosol effects in pre-industrial and present-day conditions, Schmidt showed that the high uncertainty in volcanic emissions further amplifies the uncertainty in climate forcing models due to ACI. They estimate the annual anthropogenic cloud albedo forcing to be between -1.16 and -0.86 W m^{-2}, and considering the GHG forcing is estimated around 2.3 W m^{-2}, we can see that further investigation for the indirect forcing of climate due to effusive volcanoes is needed (Myhre et al. 2013; Boucher et al. 2013).

In satellite imagery, distinctive 'volcano tracks' in aerosol and cloud properties downwind of continuously degassing volcanoes are often observed (Gassó 2008; Yuan et al. 2011). A handful of modeling and observational studies have found decreased cloud droplet size and increased cloud albedo with increased volcanic aerosol loading, providing evidence for the first indirect effect due to effusive volcanic eruptions (Gassó 2008; Yuan et al. 2011; Schmidt et al. 2012; Ebmeier et al.

2014; McCoy and Hartmann 2015; Malavelle et al. 2017). On the other hand, efforts to provide substantial evidence for the second indirect effect have been inconclusive. Overall, findings agree that continuously degassing volcanoes have a potentially large effect on the climate system that requires further investigation (Oppenheimer et al. 2011).

CHAPTER 2
THE NATURAL EXPERIMENT: KĪLAUEA VOLCANO

2.1 A Sulfur Dioxide (SO_2) Source

Kīlauea volcano on the Big Island of Hawaii (19°34' N, 155°30' W) is an active shield volcano that has been continuously degassing for over three decades. Since Kīlauea is a part of the U.S. National Park Service, its volcanic activity has been regularly monitored since 1979, giving it one of the most extensive SO_2 emission records to date (Elias et al. 1998; Elias and Sutton 2002, 2007, 2012). The current period of activity began in January 1983, with the eruption of the Pu'u 'Ō'ō vent in the East Rift Zone (ERZ), and was followed by highly variable activity, involving episodes of intense lava fountaining with emissions reaching 30,000 tonnes of SO_2 per day, to periods of eruptive pause, where emissions fell below 50 tonnes (Casadevall et al. 1987). A more recent period of enhanced activity began in March 2008, with the eruption of the Halema'uma'u vent located at the summit crater (Elias and Sutton 2012). The active eruption lasted from March through December 2008, releasing approximately 1.8 tg of SO_2 into the lower troposphere where it covered an extensive area of about 6.5 x 10^6 km^2 over the North Pacific for up to several months (Eguchi et al. 2011).

According to the latest report from the U.S. Geological Survey's Hawaiian Volcano Observatory (USGS-HVO), Kīlauea emits about 3,000 – 7,000 tonnes of SO_2 per day, for an overall average of 751,000 tonnes per year (Elias and Sutton 2012). This contribution is comparable to the amount of SO_2 attributed to all the power plants in Michigan, Minnesota, and Wisconsin combined (Hill and Baum 2001), and accounts for about 6% of the total global volcanic SO_2 (Elias and Sutton 2012). Thus, we see that although Kīlauea volcano is a natural sulfur source characterized by

variable activity, it overall contributes a significant amount especially when compared to traditional point sources, such as power plants.

2.2 Climate Setting

The Hawaiian Islands are located in the central North Pacific, more than 2,000 miles away from any major landmass or pollution source (Sanderson 1993). Its remote location in the trade wind regime allows the region to have a low background aerosol concentration that is advantageous when investigating ACI (Yuan et al. 2011). In Hawaii, climate is largely influenced by a semi-permanent subtropical high-pressure system that sits to the northeast of the state and generates the prevailing northeasterly trade wind flow that occurs throughout the year. This is especially true during boreal summer, when the trades are present between 85% to 95% of the time (Sanderson 1993). For this reason, our study focuses on the summer months of June, July, and August (JJA).

Another characteristic of the region is a strong but thin subsidence inversion that persists at an altitude near 2 km (6,560 ft) (Sanderson 1993). This trade wind inversion (TWI) acts as convective cap, limiting vertical growth of clouds. Thus, the TWI traps volcanic emissions within the MBL. Cao et al. (2007) looked at long-term radiosonde data for Hawaii from 1979 to 2003 and found that the trade wind inversion (TWI) occurred about 82% of the time with an average base height of 2,076 m (798.8 hPa). Therefore, we expect clouds in the region of the Hawaiian Islands to be contained within the lowest 2.5 km under trade wind conditions.

Overall, Hawaii's unique environment together with Kīlauea's SO_2 contribution provide an excellent opportunity to investigate ACI in a setting where sulfur is continuously emitted into a clean MBL. This natural laboratory allows for a simplified analysis of ACI in warm TCu downwind of Kīlauea volcano. Additionally, these studies can be used to explore sulfur chemistry in a setting that significantly differs from well-documented power plants (Pattantyus et al. 2018). By taking advantage of these natural experiment opportunities, we aim to improve our overall

understanding of how volcanic emissions affect clouds and climate. A handful of studies using satellite retrievals of cloud and aerosol properties to investigate ACI in TCu downstream of Kīlauea volcano exist. The following is a brief review of their findings.

For JJA 2008, Yuan et al. (2011) found clouds within the volcano tracks to have smaller cloud droplets by 3 – 8 μm, decreased precipitation rates by 30% - 80%, increased cloud-top heights by 400 – 500 m, increased optical depth by up to 9, and increased cloud fraction by up to 25%, relative to background values. Likewise, Eguchi et al. (2011) showed that polluted clouds had smaller cloud droplets by about 25% and increased cloud fractional coverage by 9.1% - 13.4% during the entire active eruption period of Halemaʻumaʻu (Mar – Dec 2008).

Instead of focusing on a high-aerosol loading event, such as with the Halemaʻumaʻu eruption mentioned previously, Ebmeier et al. (2014) used data averaged over a general 10-year period from 2002 to 2013. This study showed a decrease in cloud droplet size, ranging from 2 – 8 μm, downwind of Kīlauea. These results represent the overall net effect of Kīlauea's volcanic emissions on downstream cloud properties, and agree with previous findings from Yuan et al. (2011) and Eguchi et al. (2011). Similarly, Mace and Abernathy (2016) did not choose a specific period of enhanced activity, but instead focused directly on the region downwind of Kīlauea from 170ºW, 20ºN to 155ºW, 16ºN. The data selection spanned a 3-year period and included approximately 600 A-Train overpasses. Altogether, they found significantly higher cloud tops, comparable to the findings of Yuan et al. (2011). Both studies used Cloud-Aerosol Lidar with Orthogonal Polarization (CALIOP) data from the Cloud-Aerosol Lidar and Infrared Pathfinder Satellite Observations (CALIPSO) platform, to define cloud-top height, but with different data selection periods.

Overall, these studies agree and provide evidence for volcanic aerosol indirect effects downwind of Kīlauea. However, in a more recent study, conflicting evidence was provided and should be addressed. Malavelle et al. (2017) showed undetectable

changes in liquid water path (LWP) in clouds downwind of Kīlauea for JJA 2008, concluding that the LWP insensitivity suggests indirect aerosol effects and cloud systems that are well-buffered against changes in aerosol amount. We remind you that during that same period, Yuan et al. (2011) showed significantly suppressed precipitation and increased cloud optical depth, which would suggest a subsequent increase in LWP for in-plume clouds due to the second indirect effect. Thus, further investigation is needed to determine the magnitude of ACI from Kīlauea's aerosol plume.

2.3 Vog in Hawaii

In the Kīlauea environment, SO_2 emissions rapidly convert to sulfate aerosol, forming a plume of volcanic smog, referred to as 'vog.' Studies have found the conversion of SO_2 to sulfate to fall between 12 hours and a few days (Porter et al. 2002; Beirle et al. 2013; Pattantyus et al. 2018), while a more recent study by Kroll et al. (2015) using real-time measurements every 5 minutes suggests a plume age of 5 hours and an instantaneous oxidation rate of 2.4×10^{-6} s^{-1} at solar noon. Vog consists of SO_2 gas and both liquid and particulate sulfate, all of which can be detrimental to human health and the environment at high concentrations and prolonged periods of exposure as discussed in Section 1.1.1. The current 2018 "State of the Air" report from the American Lung Association gave Hawaii County a failing grade with respect to particle pollution. In addition, Kīlauea's plume particles have been shown to be extremely acidic with pH values within the range of battery acid, reaching as low as -0.8, although it should be noted that these values are largely influenced by the ambient moisture conditions and SO_2 emission rates (Kroll et al. 2015).

Under typical trade wind conditions, vog primarily affects nearby communities downwind of Kīlauea and along the Kona coast due to local sea-breeze circulations (Businger et al. 2015). Furthermore, under certain weather patterns, such as an approaching cold front or Kona storm, vog can become a hazard throughout the entire island chain. These wintertime disturbances result in the eastward migration

of the North Pacific High, causing a wind shift from northeasterly to southeasterly flow (Businger et al. 2015). This change tends to be associated with a period of light wind conditions, which can increase vog pollution by favoring the formation and accumulation of particulate sulfate (Kroll et al. 2015). Other factors, such as a strong capping TWI and increased volcanic activity can also enhance the severity of vog episodes and amplify the harmful impacts of vog. For these reasons, near real-time vog forecasts are provided to the public through the Vog Measurement and Prediction (VMAP) project (http://weather.hawaii.edu/vmap/). The VMAP project aims to address vog hazards from Kīlauea volcano by supplying a guidance forecast tool that can warn local communities of the upcoming vog pollution conditions. For more information on the VMAP project and how vog is observed and forecasted refer to Businger et al. (2015).

2.4 Orographic Effects

Due to the steady trade wind flow impinging on the Hawaiian Islands, orographic effects on multi-spatial scales are introduced. These effects differ from island to island due to differences in topographic features, such as terrain height, size, shape, and orientation, which influence island-scale circulations and thus over-island and island wake effects. Past studies investigating atmospheric circulations in the region of the Hawaiian Islands have generally focused on either orographic effects (Smith and Grubišić 1993; Xie et al. 2001; Yang et al. 2008; Liu et al. 2014) or aerosol effects from Kīlauea volcano (Eguchi et al. 2011; Yuan et al. 2011; Ebmeier et al. 2014; Mace and Abernathy 2016; Mallavelle et al. 2017), while a combined effect has not been thoroughly considered. By exploring clouds downwind of islands with and without a volcanic aerosol source, Ebmeier et al. (2014) showed that observed changes in cloud properties were not solely a result of orographic effects. Therefore, we must also consider Hawaii's orographic effects when investigating changes in cloud properties downwind of the Hawaiian Islands.

Under trade wind conditions, warm moist air is pushed up the slopes of Hawaii's mountainous terrain, increasing cloud frequency and rainfall along

windward slopes via orographic lifting (Yang and Chen 2008). In some cases, the terrain height may exceed the TWI (~2 km), resulting in split airflow around these mountain peaks. This is the case for the easternmost islands of Maui and the Big Island, with Haleakala at 3,055 m (10,023 ft) in east Maui, and Mauna Kea and Mauna Loa at 4,205 m (13,796 ft) and 4,169 m (13,679 ft), respectively, for Big Island summits.

2.4.1 The Mechanical Wake of the Big Island

For the Big Island of Hawaii, split airflow around the summits of Mauna Kea and Mauna Loa induce wind curls around the northern tip of Kohala and eastern tip of Puna due to orographic blocking (Figure 2.1). This ultimately results in the formation of two elongated counter-rotating quasi-steady eddies that extend off the Kona coast for about 200 km towards the west-southwest, inducing a strong westerly return flow along the wake axis (Smith and Grubišić 1993). This near-field wake effect is often referred to as the mechanical wake of the Big Island and is shown in Figure 2.2. Smith and Grubišić (1993) observed the mechanical wake using aerial observations during the 1990 Hawaiian Rainband Project (HaRP) field campaign. The southern anticyclonic eddy has been shown to have a heavy aerosol load due to the entrainment of the Kīlauea plume (Smith and Grubišić 1993). Therefore, we expect clouds downwind of the Big Island to contain aerosol from Kīlauea volcano. Although the surface wind divergence in the southern eddy suppresses cloud formation, studies have shown that the convergence in the northern clockwise eddy is much more pronounced and thus allows the formation of a cloud wake that broadens considerably downstream of the Big Island (Smith and Grubišić 1993; Liu et al. 2014). This cloud wake is often observed in satellite imagery and is likely associated with the fact that higher water vapor content is found along the wake axis due to low-level convergence (Yang and Chen 2003).

2.4.2 Cloud Trails off Kauai and Oahu

Trail cloud bands are frequently observed in satellite imagery (refer to Figure 2.2) off the west coasts of Kauai and Oahu, hereafter referred to as 'cloud trails.' During the daytime, surface heating effects allow warmer air to be transported from over-island to the wake zone via warm advection (Yang et al. 2008). The result is an increase in surface temperature in the near-island wake, which decreases surface pressure and enhances low-level convergence, favoring the formation and persistence of cloud trails. At night, as the island surface cools, cloud formation is suppressed in the wake zone due to cold advection. Using CALIPSO lidar data, Liu et al. (2015) observed this as a distinguished cloud hole below 1.6 km.

2.4.3 Maui's Makena Cloud

For the island of Maui, airflow deflection from the West Maui Mountains and orographic blocking from Haleakala induce a set of asymmetrical counter-rotating lee vortices and a westerly reverse flow (Carlis et al. 2010). Compared to the mechanical wake of the Big Island mentioned above, the main distinction is that Maui lee vortices occur primarily over land and thus are largely influenced by diurnal heating patterns. The northern cyclonic eddy, also referred to as the Maui vortex, forms in the lee of Haleakala over the Central Valley of Maui and dominates island-scale circulations (Figure 2.3). It is of particular importance since it is known to affect air pollution over central Maui by trapping biomass burning aerosols that are produced during the harvesting activities of sugarcane (Schroeder 1993; Ueyoshi et al. 1996; Carlis et al. 2010). According to Hawaiian Commercial and Sugar (HC&S), Maui's largest sugarcane producer, burning season is generally observed from March to November. HC&S estimates that about 400 acres of sugarcane are burned per week. Over time, growing concerns from local communities on Maui over the negative impacts of large corporate sugarcane operations, such as air pollution and water usage, resulted in HC&S closing all operations by late 2016. The whopping 36,000 acres of HC&S plantation land is said to be repurposed, changing directions towards a diversified agricultural model.

At the same time, there is a cloud feature, referred to as the Makena cloud, that forms daily under trade wind conditions in the lee of Haleakala, extending nearly seven miles to the southwest of Maui towards the island of Kahoolawe (refer to Figure 2.2). The cloud feature is infamous for producing overcast skies over one of Maui's most popular beaches, Makena Beach also locally referred to as Big Beach. We hypothesize that the Makena cloud will have smaller cloud droplets compared to nearby unperturbed clouds due to the increased aerosol load from the Maui vortex.

CHAPTER 3
OBSERVATIONAL AND MODEL DATA

3.1 The MODerate Resolution Imaging Spectroradiometer (MODIS)

The MODerate Resolution Imaging Spectroradiometer (MODIS) is a 36-band whiskbroom scanning radiometer aboard NASA's Terra and Aqua Earth Observing System (EOS) platforms. For this study, we use data from the Aqua satellite, which launched in 2002 and is a polar-orbiting and sun-synchronous platform, following an ascending orbit (daytime) with a 1330 equatorial local crossing time (Platnick et al. 2015). We use daytime only data for the Level-2 (L2) Atmosphere products (both Cloud and Aerosol) from Collection 6 (C6), which are available online through the Level-1 and Atmosphere Archive and Distribution System (LAADS) Distributed Active Archive Center (DAAC) website (https://ladsweb.modaps.eosdis.nasa.gov/). Additionally, auxiliary MODIS visible imagery is used from the MODIS Atmosphere L1B granule images webpage (https://modis-images.gsfc.nasa.gov/IMAGES/02_1km_main.html).

3.1.1 The MODIS Cloud Product

Cloud properties are defined using the MODIS L2 cloud product (MYD06), which provides pixel-level retrievals of cloud physical and radiative properties, for *probably cloudy* and *cloudy* pixels of the 48-bit cloud mask (MYD35) (Platnick et al. 2015). The cloud product produces 5-minute granules of data consisting of 2,030 along-track pixels, while the cloud mask is used to determine the level of confidence of cloudy contamination (*confident clear, probably clear, uncertain/probably cloudy, or cloudy*) within each pixel, and serves as the primary input for cloud property retrieval algorithms (Platnick et al. 2015). When determining the cloudiness of L1B

radiance and reflectance pixels, the cloud mask can often run into issues with tricky optical phenomena, such as the sunglint feature that appears over ocean surfaces. Threshold adjustments made in C6, have improved the occurrence of *uncertain* and *cloudy* flags for sunglint regions.

In this study, we investigate changes in six individual MODIS L2 cloud properties. Cloud-top pressure (CTP) in hPa, cloud-top temperature (CTT) in K, and cloud fraction (CF) are produced at a 5 km resolution using infrared retrieval methods. Here, MODIS uses the carbon dioxide (CO_2) slicing method to infer CTP, utilizing the differences in partial absorption within the CO_2 slicing bands from 13.3 μm to 14.2 μm. With increasing wavelengths in this range, more CO_2 is absorbed by the atmosphere causing it to become increasingly opaque to MODIS sensors. This sensitivity in spectral radiances allow clouds to appear according to their level in the atmosphere. MODIS converts CTP values into CTT, using gridded meteorological data from the National Centers for Environmental Prediction (NCEP) Global Data Assimilation System (GDAS), which provides temperature profiles every 6 hours (Derber et al. 1991).

Cloud droplet effective radius (CER) in μm, cloud optical thickness (COT), and cloud water path (CWP) in g m^{-2} are retrieved at 1 km resolution using solar reflectance techniques. This method utilizes multi-spectral reflectances in the visible, near-infrared, shortwave-infrared, and midwave-infrared, along with several thermal bands (Platnick et al. 2015). Improvements in these C6 1 km cloud parameters require corresponding 1 km geolocation data (MYD03) files, which can be obtained from the same LAADS DAAC website. This high-resolution data allows us to investigate tiny TCu clouds that cannot be resolved in MODIS Level-3 cloud properties, which have been used in previous Kīlauea studies (Eguchi et al. 2011; Yuan et al. 2011). The finer detail allows our study to better observe ACI in the TCu regime. For more information on the MODIS L2 C6 cloud products and cloud property retrieval algorithms, refer to the user guide provided by Platnick et al. (2015).

3.1.2 The MODIS Aerosol Product

The MODIS aerosol product (MYD04) provides daily L2 aerosol optical depth (AOD) data over land and ocean at a spatial resolution of 10-km. MODIS AOD is a unitless value that measures the magnitude at which particles prevent the solar beam from traveling through the atmosphere. This data allows us to identify the general location of the volcanic aerosol plume within MODIS granules and is used as a quality control check, allowing us to verify the presence of the vog plume downwind of Kīlauea volcano. AOD values less than 0.1 indicate an area of "clean" air, which is generally observed in the region surrounding the Hawaiian Islands. For additional information on the MODIS C6 algorithms used to retrieve aerosol products over land and ocean refer to Levy et al. (2013).

3.2 The Vog Measurement and Prediction (VMAP) Project Data

Collaborators of the VMAP project include efforts from a dispersion modeling team and a group responsible for emissions observations at the Hawaiian Volcano Observatory (HVO). Because our study involves the comparison of in-plume and out of plume clouds, it is essential to identify the location of Kīlauea's aerosol plume for each individual MODIS L2 granule. Although the MODIS L2 AOD is useful for providing a visual check for the presence of the volcanic plume within granules, there are considerable limitations. One of the fundamental problems is that MODIS cannot retrieve aerosol properties where sunglint is detected or where clouds are detected and masked. Since sunglint is regularly observed in Hawaii granules due to the ocean surface surrounding the Hawaiian Islands, this results in much of the MODIS aerosol data being blacked out. The absence of cloudy and sunglint pixels in MODIS aerosol products impairs the ability to determine the specific location of the Kīlauea aerosol plume within MODIS granules. In addition, MODIS AOD is retrieved at a much lower resolution than MODIS cloud properties. This is because

the Dark Target (DT) algorithm used by MODIS to retrieve aerosol products has an output grid of 135 pixels in width by 203 pixels in length, while MODIS 5 km and 1 km cloud parameters have an output grid of 270 x 406 pixels and 1354 x 2030 pixels, respectively. VMAP Vog model output is provided at a 900 m resolution. Thus, we use this high-resolution Vog model data to determine the location in latitude-longitude of the volcanic aerosol plume within MODIS granules (Figure 3.1). For our study, VMAP Vog model data during the months of June, July, and August (JJA) from 2011 – 2017 is used. The start of the data selection period was chosen based on the availability of the VMAP data.

3.2.1 SO_2 Emissions Observations

SO_2 emissions from Kīlauea volcano are regularly monitored using ultraviolet (UV) spectrometers called FLYSPECs, which measure the amount of UV light absorbed by SO_2 particles within the volcanic plume (Elias and Sutton 2012). Under trade wind conditions, vehicle-mounted FLYSPECs take measurements downwind of the Puʻu ʻŌʻō vent and summit crater along the Chain of Craters Road and Crater Rim Drive (Figure 3.2). In addition, a FLYSPEC array, consisting of 10 stationary FLYSPECs, continuously monitor the Halemaʻumaʻu vent, taking real-time measurements downwind of the summit crater every 10 seconds. For more information on how vog is monitored at HVO refer to Elias and Sutton (2012).

3.2.2 Vog Model

A regional Vog model generates 60-hour forecasts using NOAA's Hybrid Single-Particle Lagrangian Integrated Trajectory (HYSPLIT) numerical dispersion model version 4, utilizing a nested grid and including simulations for trajectory, dispersion, and pollutant concentration (Draxler and Hess 1997, 1998, 1999). A comprehensive review of the HYSPLIT Atmospheric Transport and Dispersion modeling system is provided by Stein et al. (2015). Weekly averaged SO_2 emissions data from observations at HVO, along with output from the Weather Research and Forecast (WRF) Advanced Research (AR) numerical weather prediction model, at 1

hour temporal resolution, provide the primary input for the Vog model. WRF-AR provides high-resolution wind fields and thermodynamic data, but also requires input for its initial and boundary conditions. This is provided by NCEP's Global Forecasting System (GFS) model output, along with WRF three-dimensional variational data (WRF-3D-Var). Each VMAP Vog model forecast is initialized at 00Z and 12Z. For this study, we use the hourly averaged output that is closest in time to each of the MODIS cases and integrated from the surface to 100 m above ground level. For a comprehensive review of the VMAP Vog model, including results and validation analysis, refer to Businger et al. (2015).

3.3 Ambient Air Quality Data

The Hawaii State Department of Health (HS-DOH) regularly monitors ambient level pollutants statewide, providing near real-time air quality reports available online from their website (http://hawaii.envi-beta.com/). In this study, we examine concentrations of SO_2 in ppm and $PM_{2.5}$ in μg m^{-3} using the closest hourly average to each of the MODIS cases. However, $PM_{2.5}$ was only examined for cases in JJA 2015 to 2017 due to missing data in the previous years. We note that the HS-DOH issues a data disclaimer for the records provided on their website, stating that the air quality data is still considered preliminary and has yet to be reviewed and validated by the appropriate personnel. Equipment malfunctions and other technical difficulties are listed as potential contributing factors that may result in flawed data. To address this issue, we reviewed the data and removed any clear outliers, such as negative values.

HS-DOH ambient air quality measurements are collected and reported from Hawaii's 13 statewide air-monitoring sites, in which 6 of the 13 are located on the Big Island, with stations upwind of Kīlauea volcano at Mountain View, Hilo, and Pahoa, and downwind at Pahala, Ocean View, and Kona. Other air-monitoring sites include Kahului and Kihei on Maui, Pearl City, Kapolei, Honolulu, and Sand Island

on Oahu, and Niumalu on Kauai. For a map showing the locations of the Hawaii's 13 air-monitoring sites refer to Figure 3.3.

The purpose of the ambient air quality data is to determine if there are any other noteworthy aerosol sources with respect to Kīlauea volcano, such as island surface pollution. By comparing air quality data between an upwind site (Mountain View) and downwind site (Pahala) on the Big Island, we aim to identify if there are substantial contributing sources that may affect downstream cloud properties. In addition, we include ambient $PM_{2.5}$ data from sites on Maui (Kahului and Kihei), Oahu (Pearl City), and Kauai (Niumalu) within our analysis of orographic cloud features that are also included in this study.

3.4 The Cloud-Aerosol Lidar and Infrared Pathfinder Satellite Observation (CALIPSO) Data

For our case study, we use the L2 Vertical Feature Mask (VFM) from the CALIOP sensor Version 4.10 aboard the CALIPSO platform. Vertical profiles of aerosols and clouds are provided at a 333 m spatial resolution with a 0.74 seconds temporal resolution. This data is available online through NASA's Atmospheric Science Data Center (ASDC) website (https://eosweb.larc.nasa.gov/project/calipso/lidar_l2_vfm_table).

CHAPTER 4
METHODS

4.1 Data Selection

In our study, we compared MODIS L2 cloud properties between clouds located in the volcanic plume, hereafter referred to as 'IP' clouds, and nearby clouds located out of the aerosol plume, hereafter referred to as 'OOP' clouds. MODIS cases were selected based on the following criteria: a) the Hawaiian Islands must be within the MODIS L2 granule with adequate view to the north and south of the entire island chain, b) there must be a detected aerosol plume to the southwest (downwind) of the Big Island as determined via MODIS L2 AOD, c) some clouds must be present in the area downwind of the Big Island and in the designated OOP areas, and d) the VMAP Vog model forecast must be available for the hour corresponding to each MODIS cases. Auxiliary MODIS visible images were used to filter through overpasses from JJA of 2011 – 2017, in which a total of 127 cases were identified meeting the above criteria. Because of the orbital track of the Aqua satellite, the cases were typically observed within the first hour, between 00Z and 01Z, and the last hour, between 23Z and 24Z. As mentioned in Section 3.2.2, Vog model forecasts are initialized at 00Z and 12Z. We are still able to get hourly VMAP data for the MODIS cases that fall within the first hour, because the Vog model uses the previous forecast to initialize the model in order to ensure that the vog plume is well developed to match the cloud field. Table 4.1 provides the number of cases selected for each year and shows that the distribution is relatively well spread out throughout the entire data selection period. For a complete list of MODIS cases used in this study, including the date, Julian day, and time stamp, refer to Appendix A.

4.1.1 Subsetting the MODIS Granule

To accommodate the VMAP Vog model trajectories, we used a zoomed-in region around the Hawaiian Islands, covering an area between 14ºN, 162ºW and 24ºN, 152ºW. The subset includes adequate coverage in the areas upwind and downwind of the island chain, allowing us to compare IP and OOP cloud properties. Figure 4.1 shows the original size of a MODIS L2 granule and the zoomed-in subset used in this study.

4.2 MODIS Cloud Properties

Using the data selection criteria, a total of 127 MODIS cases were selected. We compute overall and yearly averages for each of the observed MODIS cloud properties, including CER, COT, CWP, CTP, CTT, and CF, for IP and OOP clouds. Because cloud properties have been shown to vary widely between IP and OOP clouds, we also summarize our results in histograms with normalized counts on the vertical axis for each MODIS cloud property. Histograms are obtained by breaking up the distribution of each data set into equal-sized bins, in which the number of points that fall into each bin are counted. Bin boundaries are chosen for each MODIS cloud property, using the distributions that are generally observed. CER is represented by 50 bins from 1 μm to 50 μm, COT by 16 bins from 0 to 150, CWP by 20 bins from 50 g m^{-2} to 1000 g m^{-2}, CTP by 20 bins from 100 hPa to 1050 hPa, CTT by 25 bins from 195 K to 315 K, and CF by 20 bins from 0 to 1. Lastly, we normalize the counts by dividing them in each bin by the total number of observations. The purpose of the relative histograms is to provide a more complete representation of the distribution of each data set.

4.2.1 In Plume (IP) Clouds

For each individual case, we use the hourly output from the VMAP Vog model for the closest corresponding time to determine the location of the Kīlauea aerosol plume within the MODIS granule. The closest pixel of MODIS L2 cloud property data to each of the Vog model plume points is then used to calculate IP values for

each of the MODIS L2 cloud properties. Figure 4.2 shows the general location in which IP clouds are observed indicated by the green dashed line.

4.2.2 Out of Plume (OOP) Clouds

To compare cloud properties between IP and OOP clouds, we first need to distinguish any OOP areas that we wish to investigate within the dimensions of the zoomed-in MODIS granule. Altogether, we defined three OOP areas of interest. First and foremost, we chose an area upwind of Kīlauea volcano between 22ºN, 157ºW and 24ºN, 152ºW, hereafter referred to as 'OOP-1' (Figure 4.2a). Because OOP-1 is located upstream of the Hawaiian Islands and the volcanic plume source, it represents the most pristine example of OOP clouds. Clouds associated with OOP-1 have not yet been affected by Hawaii's orographic effects nor do they contain any pollution from over-island sources, such as biomass burning or dust particles generated from island agriculture. Thus, we expect OOP-1 to provide our study with the most ideal comparison between IP and OOP clouds.

We also take advantage of this opportunity to learn more about characteristic cloud features that are associated with specific islands, in which studies are either lacking or non-existent. Ultimately, we chose to explore two areas that are also located OOP, but differ in that they are affected by orographic effects and an aerosol contribution from sources (both natural and anthropogenic) on the island, such as dust, smoke, and urban pollution, hereafter referred to as 'island aerosol.' The first is an area off the west coasts of Kauai and Oahu located between 21ºN, 162ºW and 22ºN, 158.5ºW, hereafter referred to as 'OOP-2' (Figure 4.2b). OOP-2 represents the cloud trails mentioned in Section 2.4.2. Because OOP-2 clouds form via warm advection during the daytime, we expect island aerosol from Oahu and Kauai to become entrained into the cloud bands, to some degree. Secondly, we chose an area containing Maui's Haleakala summit and the island of Kahoolawe to the southwest located between 20.48ºN, 156.72ºW and 20.8ºN, 156.15ºW, hereafter referred to as 'OOP-3' (Figure 4.2c). OOP-3 represents the Makena cloud feature discussed in

Section 2.4.1. Because the Makena cloud forms over the slopes of Haleakala, where we expect there to be increased concentrations of pollution due to sugarcane burning and the Maui vortex, we expect OOP-3 clouds to contain noticeably higher amounts of aerosol than OOP-1 and OOP-2.

While OOP-1 allows us to make an important comparison between IP polluted and OOP pristine clouds, OOP-2 and OOP-3 allow us to investigate orographic clouds that contain less pollution than IP clouds, but higher concentrations than OOP-1. In conclusion, by comparing IP and three specific examples of OOP clouds (OOP-1, OOP-2, and OOP-3), we aim to learn more about how different aerosol types and amounts affect cloud properties in the region of the Hawaiian Islands.

CHAPTER 5
RESULTS AND DISCUSSION

5.1 An Illustrating Example

We present an example case on 09 July 2015 at 0010Z, in which aerosol is shown to interact with and affect clouds downwind of the Kīlauea volcano. First, we observe clouds downstream of the Big Island in MODIS/Aqua L1B visible imagery (Figure 5.1a). Next, we identify a distinct aerosol plume in MODIS/Aqua L2 AOD, originating from the Big Island and extending in the downwind (southwest) direction (Figure 5.1b), in which some of the clouds are also located. We note that the large region of missing data in Figure 5.1b is due to MODIS algorithms filtering out sunglint regions. This band of missing data is characteristic of Hawaii granules due to the reflection of sunlight off the ocean surface.

We compare corresponding HS-DOH ambient air quality reports between Mountain View (upwind) and Pahala (downwind) air-monitoring sites on the Big Island. We find SO_2 concentrations to increase downwind of Kīlauea, from 0.0009 ppm at Mountain View to 0.0214 ppm at Pahala. This is equivalent to a 2277.78% change in SO_2 concentration due to Kīlauea's volcanic input. Thus, we can validate that Kīlauea is the primary source of sulfur in the region downwind of the Big Island. This agrees with previous studies that found signature volcano tracks in satellite observations downstream of the Big Island (Yuan et al. 2011; Eguchi et al. 2011).

Using NASA's EOS Data and Information System's Worldview interactive interface (https://worldview.earthdata.nasa.gov/), we find that, for this case, the daytime (ascending) orbital track of the CALIOP/CALIPSO sensor passed through the downstream clouds observed in Figure 5.1a, roughly between 0014Z and 0015Z from a point on the CALIPSO track around 16.8ºN, 159.9ºW to 18.4ºN, 161.1ºW.

This provides a unique opportunity to examine high-resolution vertical profiles of aerosols and clouds in the region downwind of the Kīlauea volcano. From the CALIPSO VFM on 09 July 2015 from 00:04:26.0 UTC to 00:17:54.7 UTC (Figure 5.1c), in which the area of interest is represented by a yellow dashed box, we find that tropospheric aerosols (orange) and clouds (light blue) are, in fact, interacting within the lowest 2 km MBL downstream of Kīlauea. Thus, we show that the aerosol contribution from Kīlauea is actively mixing with clouds within the MBL downwind of the Big Island.

So far we've identified a case in which clouds downwind of the Big Island were shown to be located within the Kīlauea aerosol plume, and furthermore that these downstream clouds were actively interacting with the volcanic aerosols within the lowest 2 km MBL. Next, we compare IP and OOP clouds.

MODIS L2 cloud properties were extracted for the 0010Z granule. IP cloud properties were computed using the closest VMAP Vog forecast available at 0000Z, while OOP cloud properties were averaged for OOP-1, OOP-2, and OOP-3 areas. Overall, IP clouds were found to have significantly smaller cloud droplets with IP-CER values decreased by an average of 6.88 μm (Figure 5.2a), optically thicker properties with IP-COT values increased by an average of 18.44 (Figure 5.2b), higher liquid water content with IP-CWP values increasing by an average of 104.76 g m^{-2} (Figure 5.2c), higher cloud tops with IP-CTP and IP-CTT values increased by an average of 107.89 hPa and 4.66 K (Figure 5.2d, e), respectively, and larger cloud fractional coverage with IP-CF values increasing by an average of 12% (Figure 5.2f). These results provide evidence for the first and second aerosol indirect effects, and agree with previous findings from satellite retrievals of cloud properties in the Kīlauea aerosol plume (Yuan et al. 2011; Eguchi et al. 2011; Ebmeier et al. 2014; Mace and Abernathy 2016). Additional MODIS cases are needed to strengthen these findings and to provide a more complete database for further investigation of ACI in the Kīlauea aerosol plume. This allows for a more robust statistical analysis

of the impact of the Kīlauea aerosol plume on the micro- and macrophysical properties of TCu clouds.

5.2 Evidence for the Kīlauea Aerosol Plume

Surveys of MODIS/Aqua L2 AOD granules for the 127 cases included in this study showed the presence of an aerosol plume represented by increased AOD relative to background values downwind of the Big Island. This is a result of the enhanced aerosol load due to the SO_2 contribution from Kīlauea volcano. Next, hourly averaged HS-DOH ambient SO_2 concentration data is used to compute yearly averages in Table 5.1 and overall averages for Mountain View and Pahala air-monitoring sites on the Big Island. Altogether, we found SO_2 concentrations downwind of Kīlauea volcano to significantly increase, as expected, with the Mountain View site observing an overall average of 0.0012 ppm and the Pahala site 0.0361 ppm. This is equivalent to a change in ambient SO_2 concentration of over 2,000%, furthermore validating that Kīlauea is the primary sulfur source for the downstream aerosol plume observed in MODIS AOD.

5.3 Evidence for the First Indirect Effect

As discussed in Section 1.3.1, the first indirect effect occurs when an increase in aerosol concentration results in smaller and more numerous cloud droplets for an overall brighter cloud. In Section 5.2, we observed a distinct aerosol plume downwind of the Big Island in MODIS AOD granules due to the increase in aerosol load from Kīlauea volcano. Therefore, from the first indirect effect, we expect clouds located within this aerosol plume to have decreased droplet sizes and increased thickness compared to nearby clouds located OOP.

5.3.1 Cloud Droplet Effective Radius (CER)

IP clouds were found to have smaller cloud droplets than OOP clouds, with an overall average IP-CER of 15.76 μm, compared to OOP-1 with 20.77 μm, OOP-2

with 20.63 μm, and OOP-3 with 17.20 μm (Table 5.2). For the annual averages used to compute overall values, refer to Table 5.3. These results agree with previous findings from Yuan et al. (2011), Eguchi et al. (2011), and Ebmeier et al. (2014), and provide evidence for the first indirect effect. Figure 5.3a illustrates the distribution of CER observed between IP and OOP clouds. We see that the most notable difference in cloud droplet size is observed between IP and OOP-1 clouds. From the first indirect effect, we know that increased aerosol concentration leads to more available CCN and therefore smaller, more numerous cloud droplets. Therefore, this finding is consistent with the suggestion that the upwind OOP clouds (OOP-1) have lower aerosol content than clouds within the Kīlauea aerosol plume and on the lee side of islands represented in IP, OOP-2, and OOP-3.

In addition, we find that OOP-1 and OOP-2 clouds have the most similar CER distributions, with an overall difference of only 0.14 μm. This suggests that there are relatively low aerosol concentrations in the cloud trails off the west coasts of Oahu and Kauai. We also notice that OOP-3 clouds have CER distributions most comparable to IP clouds, with CER values that are 1.44 μm larger. This suggests that Maui's Makena cloud has aerosol amounts less than but most comparable to that of IP clouds.

Overall, our results show that IP clouds have significantly smaller cloud droplets compared to OOP clouds, where the biggest difference was observed between IP clouds and clouds upwind of the Hawaiian Islands, as expected. In terms of OOP clouds that form in the lee of islands and over-island, we found Maui's Makena cloud to have droplets most similar in size to IP clouds. We hypothesized in Section 2.4.3 that OOP-3 clouds would be associated with smaller droplets due to Maui's agricultural burning of sugar cane, which releases biomass burning aerosols that become trapped and entrained into the Makena cloud via the Maui vortex. We also found that clouds upwind of the Hawaiian Islands and cloud trails off the west coasts of Oahu and Kauai had very similar distributions in cloud droplet size, as

indicated in the CER values of OOP-1 and OOP-2 clouds. This observation suggests that the aerosol contribution from Oahu and Kauai is relatively low.

5.3.2 Cloud Optical Thickness (COT)

IP clouds were found to be optically thicker than OOP clouds, with an overall average IP-COT of 19.49, compared to OOP-1 with 5.26, OOP-2 with 5.86, and OOP-3 with 14.77 (Table 5.2). Figure 5.3b shows the distribution of COT observed between IP and OOP clouds. These results agree with findings from Yuan et al. (2011) and provide evidence for the first indirect effect. Overall, we observed the biggest difference to be between IP clouds and OOP-1, which corresponds to the CER relationship described above. We also find OOP-1 and OOP-2 clouds to have nearly identical COT distributions, with a difference in overall COT of only 0.6. This also corresponds with the CER relationship, in which OOP-2 clouds had slightly smaller droplets than OOP-1 clouds. In addition, we see that again OOP-3 clouds are most comparable to IP clouds, with COT values that are smaller by a value of 4.72.

5.4 Evidence for the Second Indirect Effect

As mentioned in Section 1.3.2, the second indirect effect subsequently follows the first indirect effect and occurs when the smaller cloud droplets lead to suppressed precipitation, higher cloud tops, and overall increased cloud amount and lifetime. Therefore, from the second indirect effect, we expect IP clouds to have increased liquid water amounts, increased cloud heights, and increased cloud fractional coverage compared to OOP clouds.

5.4.1 Cloud Water Path (CWP)

IP clouds were shown to have increased liquid water content than OOP clouds, suggesting drizzle suppression effects, as expected by the second indirect effect. We found an overall average IP-CWP of 174.11 g m^{-2}, compared to OOP-1 with 59.34 g m^{-2}, OOP-2 with 60.10 g m^{-2}, and OOP-3 with 122.81 g m^{-2} (Table 5.2). Figure 5.3c

illustrates the distribution of CWP observed between IP and OOP clouds. These findings agree with results from Yuan et al. (2011), who found decreased precipitation efficiency from the CloudSat precipitation product, but deviate from the conclusions included in the supplementary information of Mallavelle et al. (2017), in which anomalies in MODIS liquid water path were found to be only "marginally influenced" and thus "invariant" despite the increase in aerosol loading.

We also found that the relationships observed in CER and COT were well-reflected in CWP values, with IP-CWP being closest to OOP-3 values, but furthest from OOP-1, along with OOP-1 and OOP-2 values sharing the closest relationship with a difference of only 0.76 g m^{-2}.

5.4.2 Cloud-Top Pressure (CTP)

IP clouds were observed to have higher cloud tops compared to OOP clouds, with an overall average IP-CTP of 788.17 hPa, compared to OOP-1 with 864.49 hPa, OOP-2 with 829.31 hPa, and OOP-3 with 812.11 hPa (Table 5.2). It is important to note that lower CTP values indicate higher cloud tops since atmospheric pressure decreases with height. Figure 5.3d shows the distribution of CTP observed between IP and OOP clouds. These findings agree with Yuan et al. (2011) and Mace and Abernathy (2016), and provide evidence for the second indirect effect.

Additionally, we found that the relationships observed in CER, COT, and CWP were well-reflected in CTP values, with IP-CTP being closest to OOP-3 values, but furthest from OOP-1, along with OOP-1 and OOP-2 values sharing the closest relationship with a difference of only 35.18 hPa.

5.4.3 Cloud-Top Temperature (CTT)

Likewise, IP-CTT was found to be lower than OOP clouds, following the same pattern as CTP, with an overall average IP-CTT of 281.76 K, compared to OOP-1 with 284.94 K, OOP-2 with 283.70 K, and OOP-3 with 282.79 K (Table 5.2). This provides further evidence for higher cloud tops in IP clouds, as expected by the

second indirect effect. Again, we emphasize that lower CTT values indicate higher cloud tops since atmospheric temperature decreases with height. In addition, we expect this close relationship between MODIS CTP and CTT, since we know CTT is generated from CTP values in MODIS algorithms. Figure 5.3e shows the distribution of CTT observed between IP and OOP clouds. These findings consequently agree with Yuan et al. (2011) and Mace and Abernathy (2016), and follow the same patterns observed and noted in CER, COT, CWP, and CTP.

5.4.4 Cloud Fraction (CF)

IP clouds were shown to have increased cloud fractional coverage compared to OOP clouds, with an overall average IP-CF of 53%, compared to OOP-1 with 44%, OOP-2 with 37%, and OOP-3 with 50% (Table 5.2). Figure 5.3f shows the distribution of CF observed between IP and OOP clouds. This agrees with findings from Yuan et al. (2011) and Eguchi et al. (2011). Although these results suggest IP clouds to have increased cloud amount, as expected by the second indirect effect, there are a couple of things to take into consideration. First is the size of the area being investigated (IP, OOP-1, OOP-2, or OOP-3) relative to one another. For instance, in terms of OOP clouds, OOP-3 covers the smallest area, followed by OOP-2, and lastly OOP-1. Because OOP-3 was chosen to represent the Makena cloud feature, it is associated with a smaller area that increases the likelihood of higher CF values. This is entirely different from the IP area, which is determined by the vog plume dispersion and location based on the VMAP Vog model forecast for each individual case. Another factor is the typical size and extent of the cloud features associated with each area. Both the size of the area of interest and the extent of the cloud feature may affect changes in CF values.

5.5 Considering Over-Island Sources

In addition to MODIS cloud and aerosol products, we also included $PM_{2.5}$ concentration data from the following HS-DOH air-monitoring sites: Mt. View (upwind) and Pahala (downwind) on the Big Island, Kahului and Kihei on Maui,

Pearl City on Oahu, and Niumalu on Kauai. The closest hourly average to each MODIS case was used to calculate the yearly averages (refer to Table 5.4) and overall values used in this study. Missing data from 2011 – 2014 along with the fact that the data remains in the preliminary stages needs to be taken into consideration when analyzing our findings. For these reasons, we present our results as more of a reference with respect to our previous findings in MODIS cloud properties. The cases in which data was missing or removed are indicated in red. Also, cases in which noticeably higher $PM_{2.5}$ concentrations (> 10 μg m^{-3}) were observed are highlighted in yellow.

5.5.1 Aerosol Contribution for IP Clouds

Overall, we found particle pollution to substantially increase from Mt. View to Pahala, with an overall $PM_{2.5}$ concentration of 2.52 μg m^{-3} observed at Mt. View and 6.74 μg m^{-3} at Pahala. This suggests that between Mt. View and Pahala sites, which is about a 32.12-mile distance, the ambient $PM_{2.5}$ concentration increases by 167.46% due to Kīlauea's volcanic input. Under trade wind conditions, we expect most of this aerosol load to be carried downwind of the Big Island, creating a plume of increased aerosol concentrations, which we found to be reflected in MODIS/Aqua AOD granules. In addition, the mechanical wake of the Big Island is responsible for transporting volcanic aerosols from Kīlauea to the wake zone, which would also contribute to the downstream aerosol plume. This was shown by Smith and Grubišić (1993) with the high aerosol load found in the southern eddy of the mechanical wake. Moreover, we assume that this volcanic aerosol plume becomes entrained into clouds downwind of the Big Island (IP clouds) to some degree. Lastly, we hypothesize that the amount of aerosol introduced into IP clouds is likely higher than the values provided by the downwind ambient $PM_{2.5}$ concentrations due to the SO_2 conversion to sulfate that occurs further downwind from Pahala. Further investigation is needed to determine the role of each mechanism in contributing increased aerosol amounts to IP clouds.

5.5.2 Aerosol Contribution for OOP-2 Clouds

For OOP-2 clouds that represent the cloud trails feature, we examine air quality data for the islands of Oahu and Kauai. We find an overall $PM_{2.5}$ concentration of 2.94 μg m^{-3} for the Pearl City site on Oahu and 2.81 μg m^{-3} for the Niumalu site on Kauai. Since we chose to group both cloud trails in this study, we also computed the overall average and find the combined ambient $PM_{2.5}$ concentration from Oahu and Kauai to be 2.88 μg m^{-3}. Knowing that Oahu is the most populated of the Hawaiian Islands, with a population over 15 times that of Kauai, we expected to see a more substantial difference in local pollution sources reflected in the ambient $PM_{2.5}$ data. Instead, the aerosol contribution between Oahu and Kauai were found to be relatively comparable, with an overall difference of only 0.13 μg m^{-3}. Because cloud trails in OOP-2 form and become anchored in the wake zone during the daytime due to air moving from over-island to the wake zone via warm advection, we expect some of this island aerosol from Oahu and Kauai to become introduced into their corresponding cloud trails.

5.5.3 Aerosol Contribution for OOP-3 Clouds

For OOP-3 clouds that represent the Makena cloud feature, we examine air quality data from the two air-monitoring sites available on the island of Maui. The Kahului site is located upwind of central Maui and the Kihei site downwind (refer to Figure 2.3). Overall, we find an average $PM_{2.5}$ concentration of 4.13 μg m^{-3} from Kahului and 4.58 μg m^{-3} from Kihei, for an average of 4.36 μg m^{-3}. The slight increase observed from Kahului to Kihei is expected since Kahului is located on the windward coast and thus would likely observe cleaner air conditions. However, it is still a higher concentration than Mt. View, Pearl City, and Niumalu. This may be related to the Maui vortex circulation that has been associated with trapping sugarcane burning aerosols and increasing pollution over the Central Valley of Maui. This would explain the relatively high $PM_{2.5}$ concentrations found at the Kahului and Kihei sites.

In addition, we see that the average $PM_{2.5}$ concentration is less than the value from Pahala that is associated with IP clouds, but greater than the value from Pearl City and Niumalu that is associated with OOP-2 clouds. This suggests that IP clouds exist in an area characterized by the highest aerosol amounts, followed by OOP-3, OOP-2, and lastly OOP-1. We assume that under trade wind conditions, as the airflow splits around Haleakala, the increased aerosol load over the Central Valley becomes introduced into the Makena cloud.

From the yearly $PM_{2.5}$ values shown in Table 5.4, we see that the maximum concentration was observed in 2015 at the Kihei site with an average of 9 $\mu g\ m^{-3}$. This value significantly decreased in 2016 by 7.36 $\mu g\ m^{-3}$ and then increased once again in 2017 by 1.44 $\mu g\ m^{-3}$. According to local news reports, we find that all of Maui's sugarcane operations shut down by late 2016. This explains the sharp drop in $PM_{2.5}$ concentrations observed from 2015 to 2016 and suggests that the sugarcane burning aerosol was a major source of pollution over central Maui. The increase observed in 2017 may be related to the repurposing and development of the 36,000 acres of plantation land.

5.5.4 Comparing $PM_{2.5}$ Data to MODIS Cloud Properties

Overall, we found the largest ambient $PM_{2.5}$ concentration to be associated with the Big Island, as expected from MODIS/Aqua AOD, followed by Maui, and lastly Oahu and Kauai. Our findings suggest that the enhanced concentrations observed at Pahala on the Big Island are largely a result of the input from Kīlauea volcano. Moreover, we expect this high aerosol load to be entrained into clouds downwind of the Big Island (IP clouds) via trade wind flow and the southern eddy of the mechanical wake. We also expect the relatively high ambient $PM_{2.5}$ concentrations observed in Maui to become introduced into OOP-3 clouds. Our findings suggest that the Maui vortex traps biomass burning pollution over the Central Valley, where the split airflow around Haleakala likely plays a role in introducing some of the aerosol into the area of Makena cloud formation. Lastly, we expect the relatively

low ambient aerosol concentrations observed over Oahu and Kauai to be associated with the cloud trails in OOP-2 clouds due to daytime warm advection bringing air over-island into the wake zone, where OOP-2 clouds are observed.

In Section 5.3, we found IP clouds to have smaller droplets, optically thicker properties, increased liquid water content, higher cloud tops, and increased cloud fractional coverage compared to OOP clouds, providing evidence for the first and second indirect effects. These findings suggest that IP clouds have the highest aerosol load, which agrees with our ambient $PM_{2.5}$ data analysis. We also identified relationships between IP, OOP-1, OOP-2, and OOP-3 clouds. First, OOP-3 clouds were found to have properties closest to IP clouds, which suggests that the Makena cloud should be associated with the second largest aerosol load. Second, we found OOP-1 and OOP-2 clouds to be the extremely comparable overall, suggesting OOP-2 cloud trails to be associated with relatively low aerosol concentrations. Similarly, both relationships agree with the current $PM_{2.5}$ analysis.

In this section, our findings from the preliminary HS-DOH ambient $PM_{2.5}$ data showed that IP clouds experienced the highest aerosol concentrations, followed by OOP-3, OOP-2, and lastly OOP-1 due to a lack of over-island sources upwind of the Hawaiian Islands. These results agree with our overall findings in MODIS cloud properties, further strengthening our evidence for the first and second indirect effects.

CHAPTER 6
SUMMARY

6.1 Conclusions

In this study, we investigated ACI in the region of the Hawaiian Islands by comparing MODIS L2 cloud properties between IP and OOP clouds (OOP-1, OOP-2, and OOP-3), for a total of 127 cases. One of the unique aspects of this study is that we use high-resolution Vog model results to determine the location of the Kīlauea aerosol plume in each individual MODIS granule. In addition, we consider both aerosol effects and orographic effects in our data analysis. This is important since previous cloud studies in the region of the Hawaiian Islands have attributed changes in downwind cloud properties to either aerosol effects from Kīlauea volcano or island-wake effects, although Ebmeier et al. (2014) suggested that cloud modification downwind of islands is not entirely a result of orographic effects. Thus, we highlight the importance of considering how both aerosol indirect effects and orographic effects play a role in modifying clouds downstream of the Hawaiian Islands, instead of using the either-or approach previously taken. For these reasons, we chose to look at two orographic cloud features in the cloud trails of OOP-2 and Makena cloud of OOP-3, in addition to the upstream pristine clouds represented in OOP-1. This allows us to compare orographic clouds that form over-island (OOP-3) and in the wake of the islands (IP and OOP-2), and furthermore explore how differing aerosol amounts associated with these clouds may affect changes in cloud properties. The following is a summary of our results:

- Preliminary ambient air quality data verified that Kīlauea volcano is the primary source of the aerosol plume observed downwind of the Big Island in MODIS/Aqua L2 AOD. Yuan et al. (2011) and Eguchi et al. (2011) identified similar volcano tracks in AOD and SO_2 downstream of the Big Island.

- IP clouds were found to have decreased droplet sizes by 1.44 – 5.01 μm and increased thickness with COT values increasing by 4.71 – 14.22 compared to OOP clouds, providing evidence for the first indirect effect.

- IP clouds were shown to have increased liquid water content by 51.3 – 114.77 g m^{-2}, higher cloud tops by 23.94 – 76.32 hPa or 1.03 – 3.18 K, and increased cloud fractional coverage by 3% – 16% compared to OOP clouds, providing evidence for the second indirect effect.

- Because upstream pristine clouds in OOP-1 lack an island aerosol source, the comparison between IP and OOP-1 clouds provides the most convincing evidence for aerosol indirect effects.

- Overall, we found that the relationships established in MODIS cloud properties were well-reflected in the preliminary $PM_{2.5}$ data. Furthermore, our findings showed that the higher ambient $PM_{2.5}$ concentrations were associated with more pronounced aerosol indirect effects.

- Our findings suggest that orographic effects likely play a significant role in introducing island aerosol into the observed cloud features in IP, OOP-2, and OOP-3 clouds.

- Another relationship that was observed in this study is that the islands with the largest topographic features, such as Mauna Kea and Mauna Loa on the Big Island and Haleakala on Maui, were associated with the most pronounced aerosol indirect effects. It can be argued that the larger orography produces a more significant convergence zone, which in turn is responsible for the changes observed in downwind cloud properties. These convergence zones that form in the lee of large orography are often associated with increased cloudiness and precipitation. One of the issues with this is that we observe increased liquid water content in IP clouds, which suggests drizzle suppression and not increased rainfall. In addition, the significant

decrease in droplet sizes found in IP clouds cannot be explained by orographic effects. However, there is a possibility that some of the changes observed in downwind cloud properties are associated with orographic effects to some degree. Further investigation is needed to untangle the roles of aerosol indirect effects and orographic effects in determining downstream cloud properties.

6.2 Future Work

The results and conclusions in this study provide ample evidence for a complex system of interactions between the Kīlauea aerosol plume and clouds downwind of the Hawaiian Islands. These findings lead to further questions and highlight the need for additional research and future studies focusing on Kīlauea volcano:

- Using similar data sets as this study, we encourage utilizing the SO_2 and SO_4 concentration data that are included in VMAP Vog forecasts. The inclusion of these data may help to establish more concrete relationships between aerosol loading and observed changes in cloud properties attributed to aerosol indirect effects. In addition, we recommend splitting up the cloud trails represented in OOP-2 off the west coasts of Oahu and Kauai. Although preliminary $PM_{2.5}$ data showed similar over-island aerosol contributions from Oahu and Kauai, it may be beneficial to further investigate these findings via changes in MODIS cloud properties for individual cloud bands. Because the HS-DOH ambient air quality data is considered preliminary, further investigation is appropriate in verifying these results.
- One of the background features of the region that should be further investigated is the role of the TWI in determining cloud-top properties. Zhang et al. (2012) looked at radiosonde and lidar data, and found the average cloud-top height in the region of the Hawaiian Islands to be strongly linked to the average TWI base height. It would be interesting to examine how the height of the TWI in each case correlates with values of MODIS cloud-top height.

- Additional data sets that were not used in this study, but should be considered in future work include precipitation data from the Tropical Rainfall Measuring Mission (TRMM) precipitation radar, MODIS/Aqua SST data, and HC&S sugarcane burn schedule. Overall trends in Kīlauea's SO_2 emission rates and HS-DOH $PM_{2.5}$ concentrations for 2011 – 2014 would also benefit future work, although these data sets were either flawed or unavailable at the time of this study.
- On 04 May 2018, Kīlauea volcano erupted, marking a new period of enhanced activity with a series of earthquakes, including one with a relatively large magnitude of 6.9, the opening of multiple fissures in Leilani Estates, and intense lava fountaining. More than five weeks later, it is estimated that over 600 homes have been destroyed and more than 2,500 people have been displaced, although these numbers continue to grow at an alarming rate as Kīlauea's newsworthy activity continues to be monitored. Big Island communities suffer from dangerously high levels of SO_2 and lava haze or 'laze,' which is produced when lava meets seawater. Overall, this provides a rare opportunity to study a sudden, significant increase in aerosol loading due to Kīlauea volcano. Previous studies focused on the March 2008 eruption at the summit crater, but unfortunately VMAP Vog model data does not extend that far back. The current eruption provides a valuable chance to investigate a high aerosol loading event using VMAP data that was previously not possible.
- Ultimately, we identify that there are further observational needs that can only be met through in-situ measurements collected in the efforts of a field campaign. A project of this magnitude would involve near and far-field aerial sampling, allowing researchers to simultaneously investigate cloud properties, aerosol properties, and sulfur chemistry. In addition to learning more about ACI, the data could help improve our understanding of some of the broader effects of vog in the region of the Hawaiian Islands. This type of project would be the second

field-campaign dedicated to atmospheric sciences in the region of the Hawaiian Islands since the Hawaiian Rainband Project (HaRP) of 1990.

TABLES

Year	# of Cases
2011	16
2012	19
2013	16
2014	22
2015	15
2016	15
2017	24
Total	127

Table 4.1. Number counts of MODIS cases included in the study from JJA 2011 – 2017, totaling 127 cases.

	2011	2012	2013	2014	2015	2016	2017
				SO_2 (ppm)			
Mt. View	0.0006	0.0009	0.0016	0.0024	0.0006	0.0017	0.0007
Pahala	0.0479	0.0421	0.0248	0.0297	0.0243	0.0496	0.0346

Table 5.1. HS-DOH ambient air quality data for the Big Island, showing SO_2 concentrations in ppm from Mountain View (upwind) and Pahala (downwind) air-monitoring sites.

	CER (μm)	COT	CWP (g/m²)	CTP (hPa)	CTT (K)	CF
IP	15.76	19.48	174.11	788.17	281.76	0.53
OOP-1	20.77	5.26	59.34	864.49	284.94	0.44
OOP-2	20.63	5.86	60.10	829.31	283.70	0.37
OOP-3	17.20	14.77	122.81	812.11	282.79	0.50

Table 5.2. Overall averages of MODIS/Aqua L2 cloud properties for IP and OOP (OOP-1, OOP-2, and OOP-3) clouds.

	2011	2012	2013	2014	2015	2016	2017
Cloud Droplet Effective Radius (μm)							
IP	18.14	12.96	13.67	15.22	14.90	14.28	20.52
OOP-1	20.77	18.96	23.68	21.39	22.85	21.84	22.39
OOP-2	23.51	17.82	24.64	26.08	21.62	24.27	27.98
OOP-3	21.91	14.39	14.41	17.03	17.21	18.38	15.88
Cloud Optical Thickness							
IP	17.30	21.31	17.82	18.95	23.18	30.78	15.06
OOP-1	5.26	7.54	5.52	5.18	5.33	6.52	6.31
OOP-2	4.98	6.69	4.99	4.58	5.99	5.40	4.82
OOP-3	11.93	16.12	16.59	12.71	16.92	15.74	14.66
Liquid Cloud Water Path (g/m^2)							
IP	168.84	177.71	140.24	162.83	188.68	266.56	147.77
OOP-1	59.34	86.10	60	58.27	44.02	73.44	61.58
OOP-2	58.44	62.09	58.68	50.49	68.85	44.38	64.58
OOP-3	108.48	110.81	130.59	125.72	135.50	116.87	130.49
Cloud-Top Pressure (hPa)							
IP	744.29	863.33	767.83	735.07	758.31	705.24	668.84
OOP-1	849.63	900.73	800	845.96	888.79	902.42	864.82
OOP-2	879.63	922.12	802.34	795.11	877.54	819.06	770.71
OOP-3	755.11	873.44	828.92	770.23	819.54	819.58	825.43
Cloud-Top Temperature (K)							
IP	278.63	288.65	279.29	277.12	281.12	272.93	269.71
OOP-1	282.57	288.04	280.09	283.86	287.43	288.12	284.94
OOP-2	287.05	290.61	279.94	280.18	287.59	281.05	277.76
OOP-3	278.19	289.28	284.86	279.25	285.08	285.17	285.39
Cloud Fraction							
IP	0.59	0.48	0.56	0.58	0.49	0.59	0.59
OOP-1	0.45	0.44	0.44	0.45	0.37	0.51	0.41
OOP-2	0.36	0.30	0.39	0.38	0.30	0.41	0.43
OOP-3	0.52	0.44	0.43	0.49	0.59	0.58	0.50

Table 5.3. As in Table 5.2, but presented in annual averages from 2011 – 2017.

	2015	2016	2017
	$PM_{2.5}$ (μg/m³)		
Mt. View (Big Island)	0.786	5.357	1.421
Pahala (Big Island)	7.933	6.533	5.75
Kahului (Maui)	4.267	3.467	4.667
Kihei (Maui)	9	1.643	3.083
Pearl City (Oahu)	5.333	1.067	2.417
Niumalu (Kauai)	3	2.067	3.364

Table 5.4. HS-DOH ambient air quality data available from 2015 – 2017 showing $PM_{2.5}$ concentrations in μg m^{-3} from the air-monitoring sites used in this study.

FIGURES

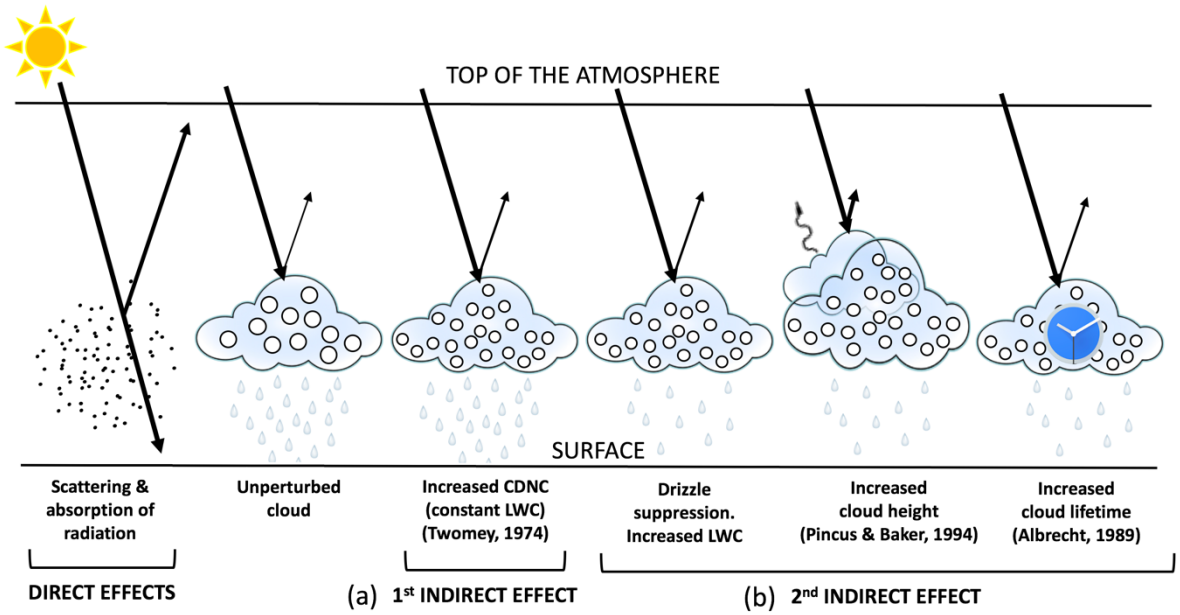

Figure 1.1. Schematic diagram of the radiative interactions between aerosols and clouds (adapted from Figure 1.1 in Haywood and Boucher 2000), including aerosol direct effects, (a) the first indirect effect, and (b) the second indirect effect.

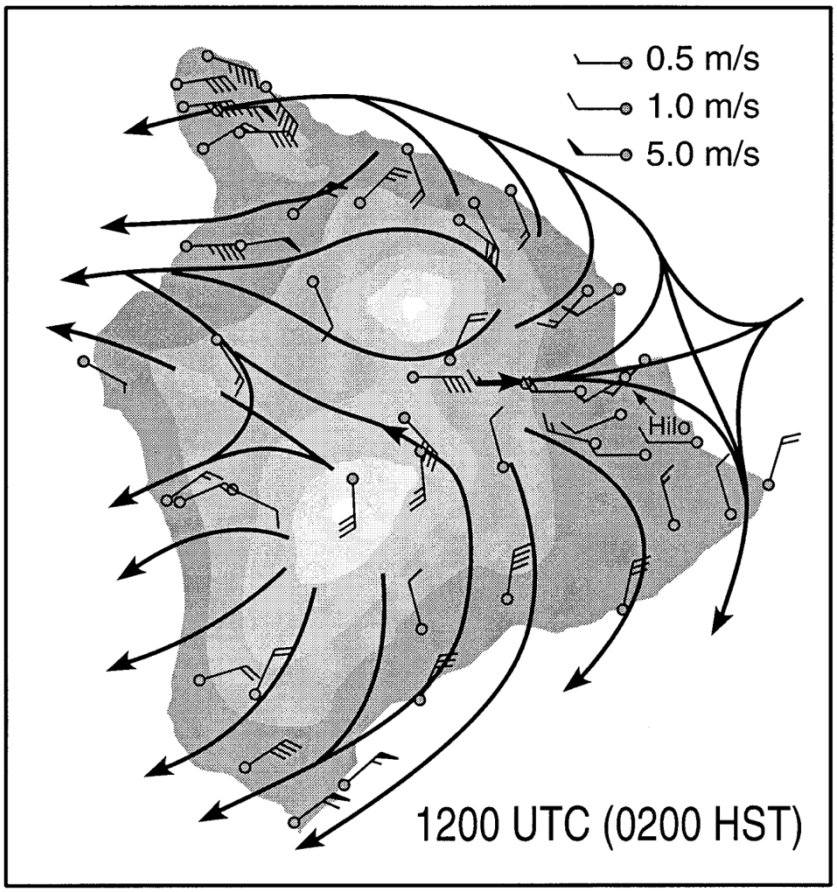

Figure 2.1. Surface streamlines under typical trade wind conditions for the Big Island, illustrating the split airflow around Mauna Kea and Mauna Loa summits, and wind curls around the northern and eastern tips of the island (Figure 12 in Kodama and Businger 1998; adapted from Chen and Nash 1994).

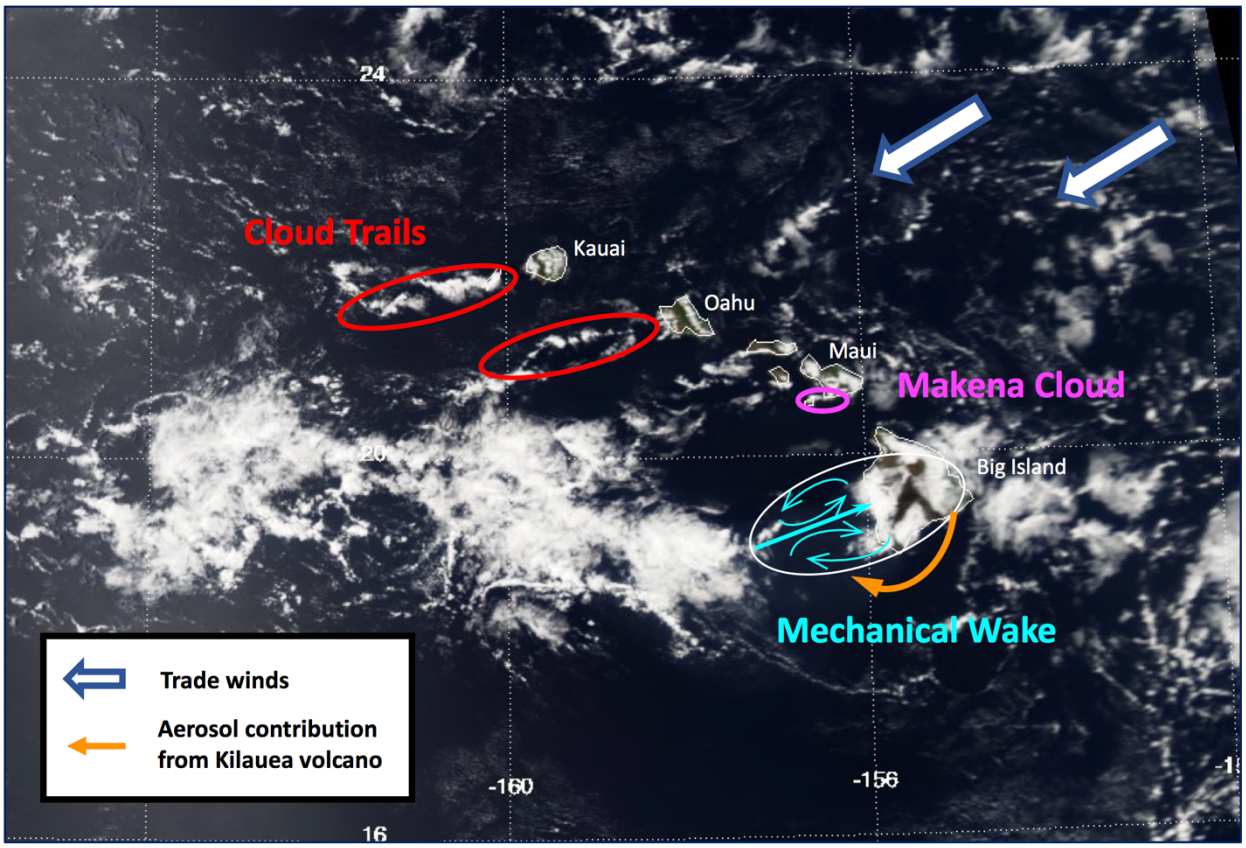

Figure 2.2. MODIS/Aqua visible imagery showing the signature orographic features discussed in this study, including the mechanical wake of the Big Island, the thermally-enhanced cloud trails off the west coasts of Oahu and Kauai, and Maui's Makena cloud.

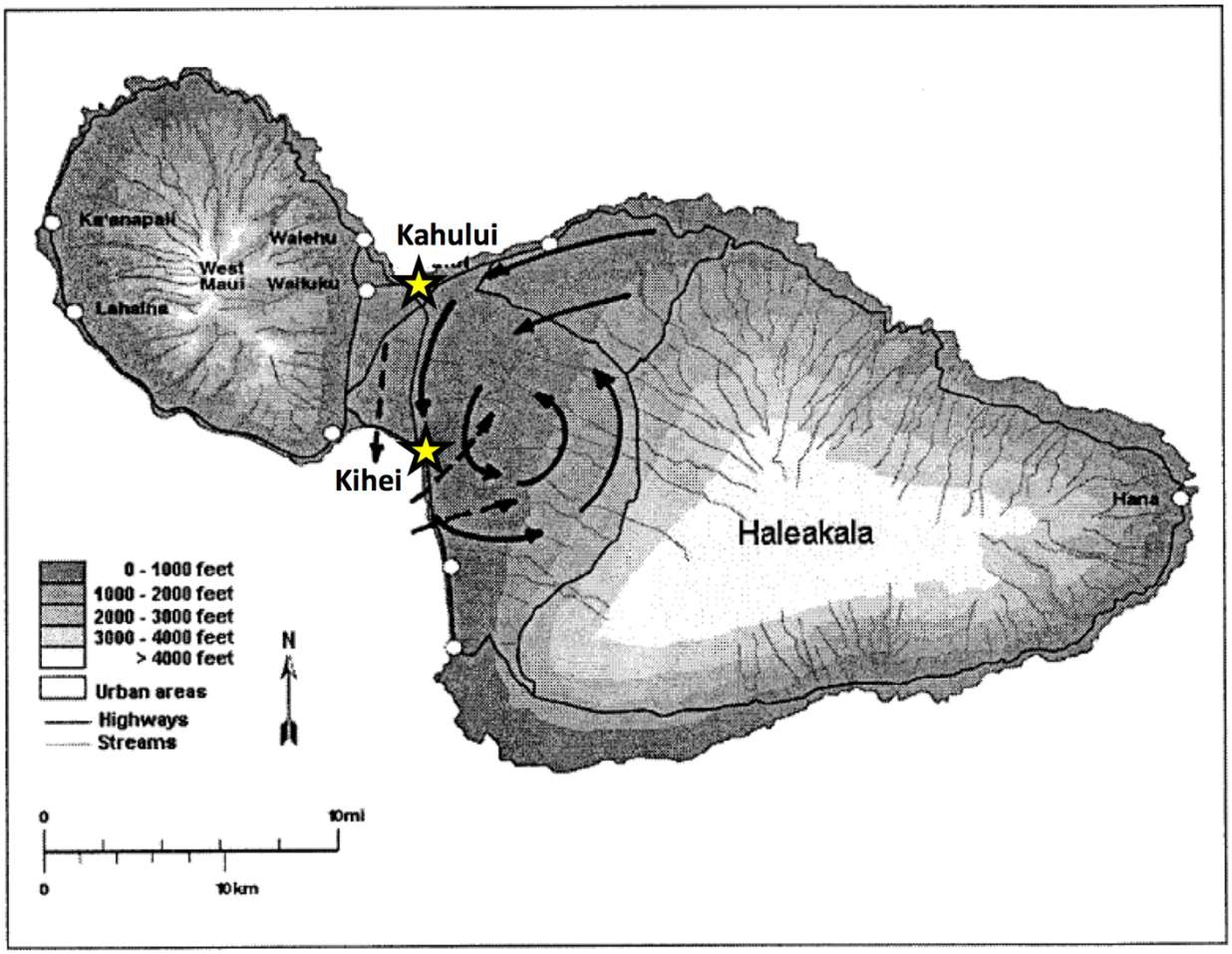

Figure 2.3. Streamlines illustrating the Maui vortex circulation that forms over the Central Valley of Maui under trade wind conditions due to surface heating and orographic effects (Figure 13 in Kodama and Businger (1998) adapted from Leopold (1949)). The locations of the two HS-DOH air-monitoring stations are shown (yellow star) for reference.

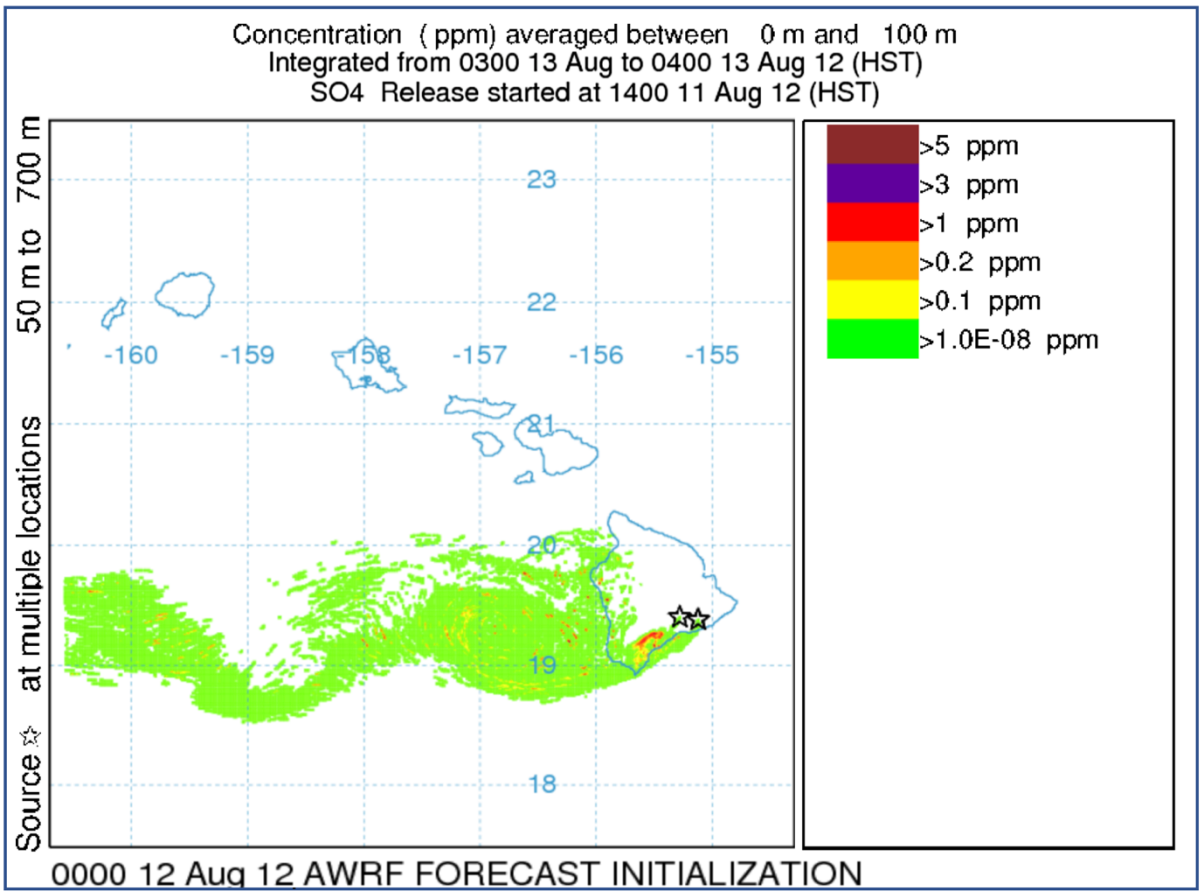

Figure 3.1. An example of a VMAP Vog model forecast initialized at 00Z on 12 August 2012 that is 38 hours out, showing predicted SO_4 concentrations in ppm and plume location.

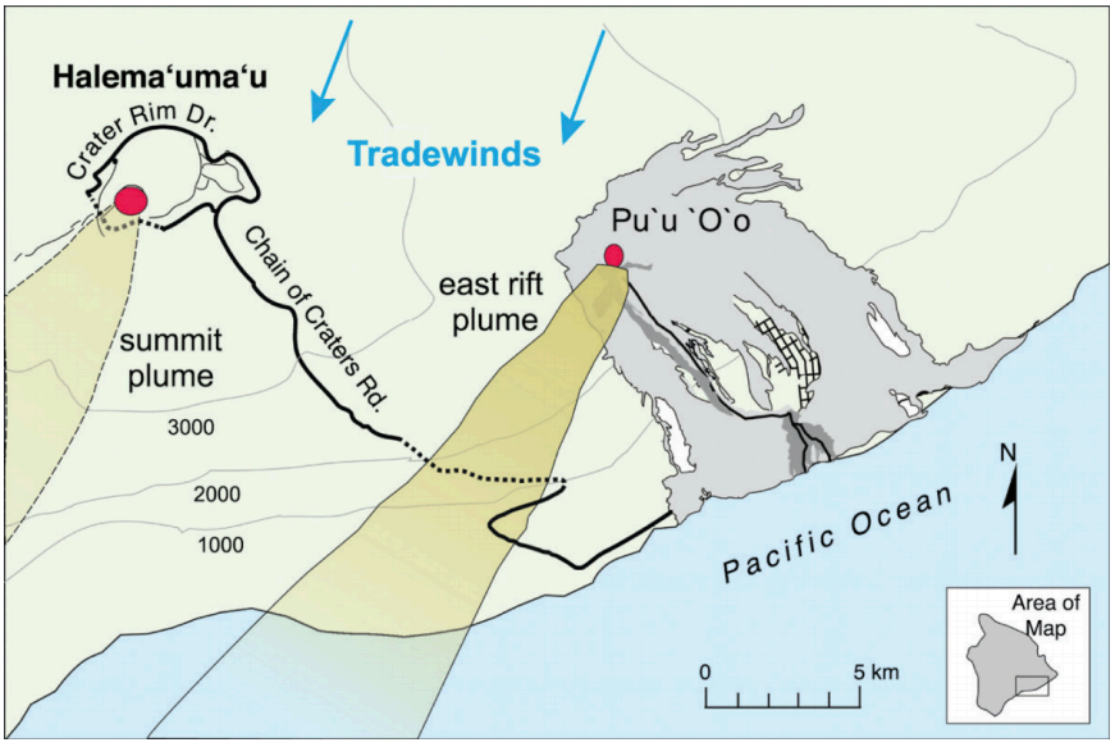

Figure 3.2. Map showing the path used under trade wind conditions for downwind SO_2 measurements from vehicle-mounted FLYSPECs along the Chain of Craters Road and Crater Rim Drive (adapted from Businger et al. 2015).

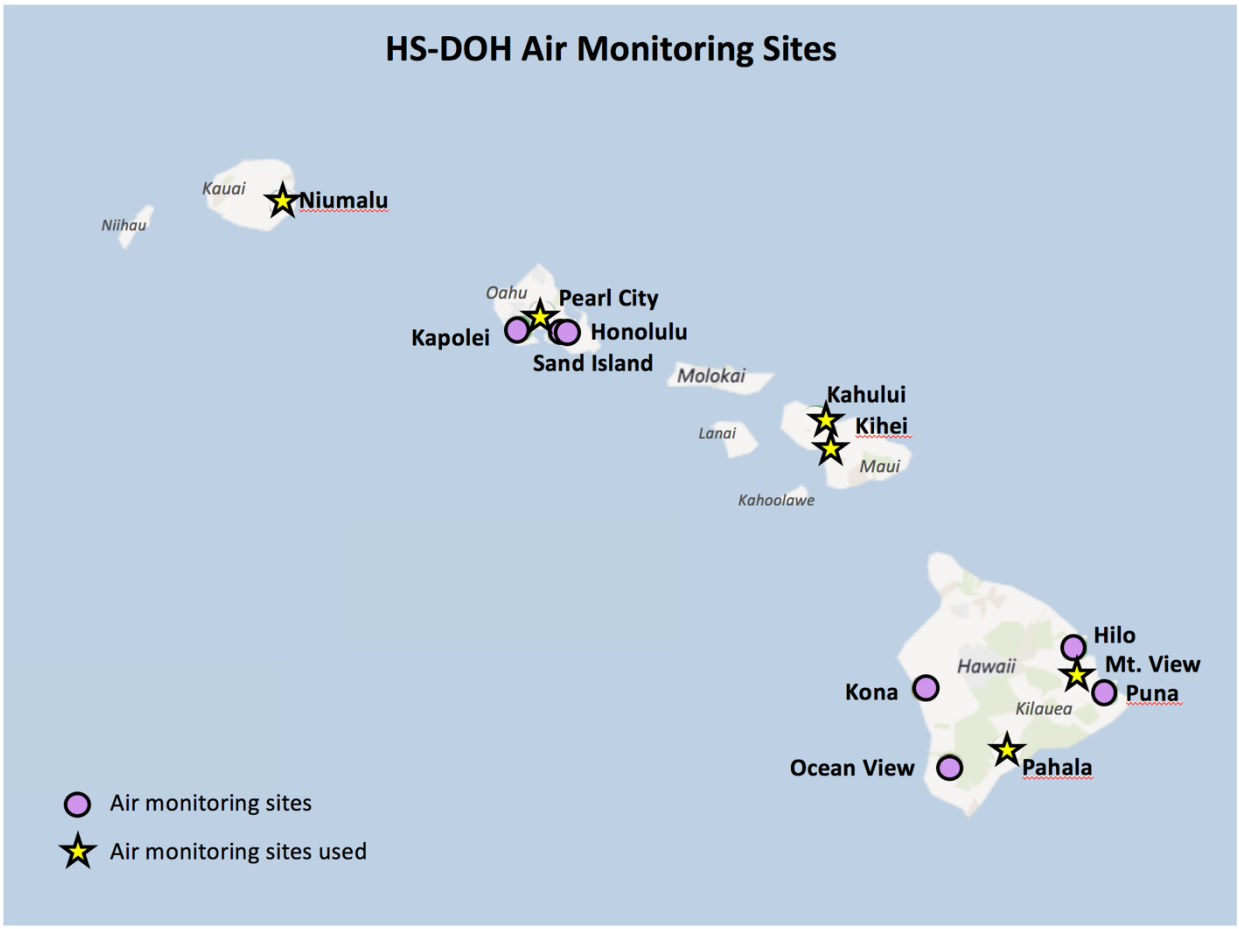

Figure 3.3. Locations of the 13 statewide HS-DOH air-monitoring sites.

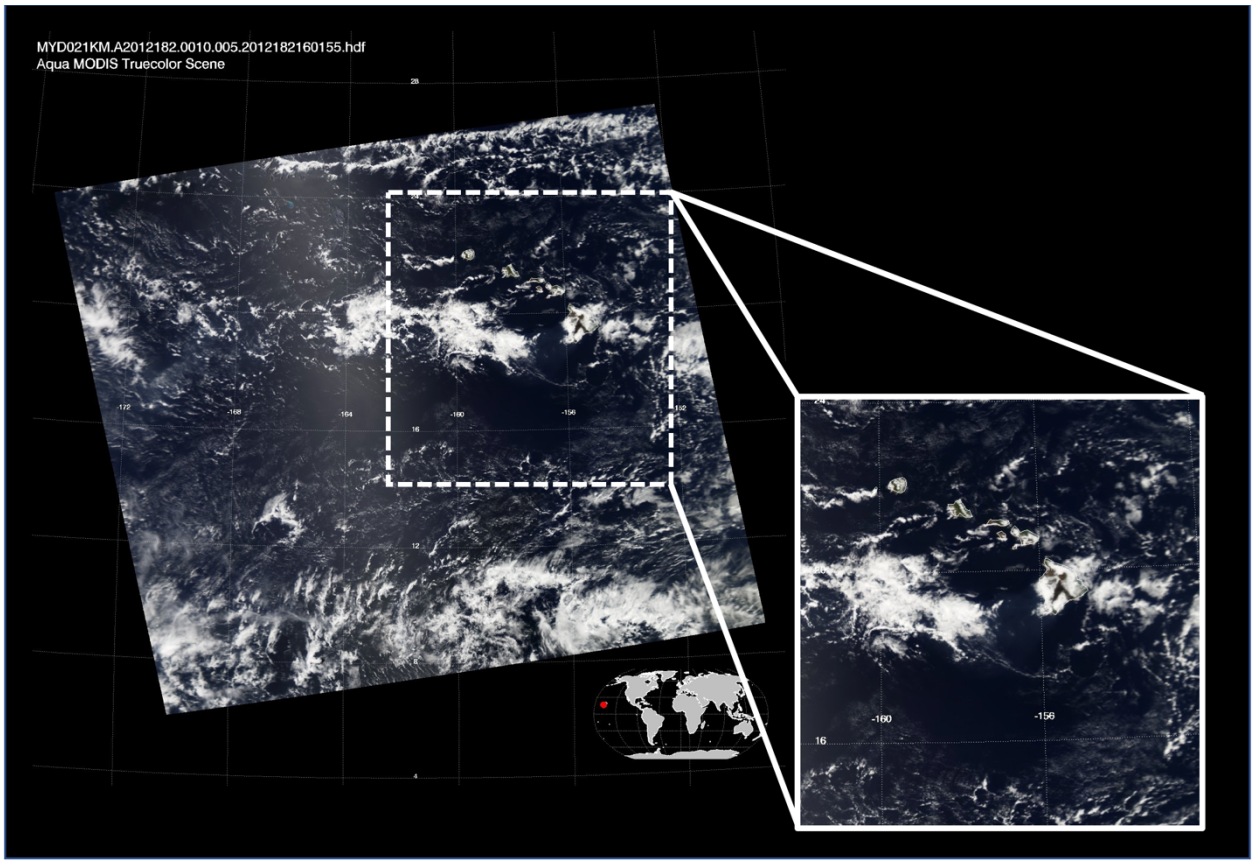

Figure 4.1. MODIS/Aqua visible imagery from 30 June 2012 at 0010Z, showing the zoomed-in subset used in this study to accommodate VMAP trajectories.

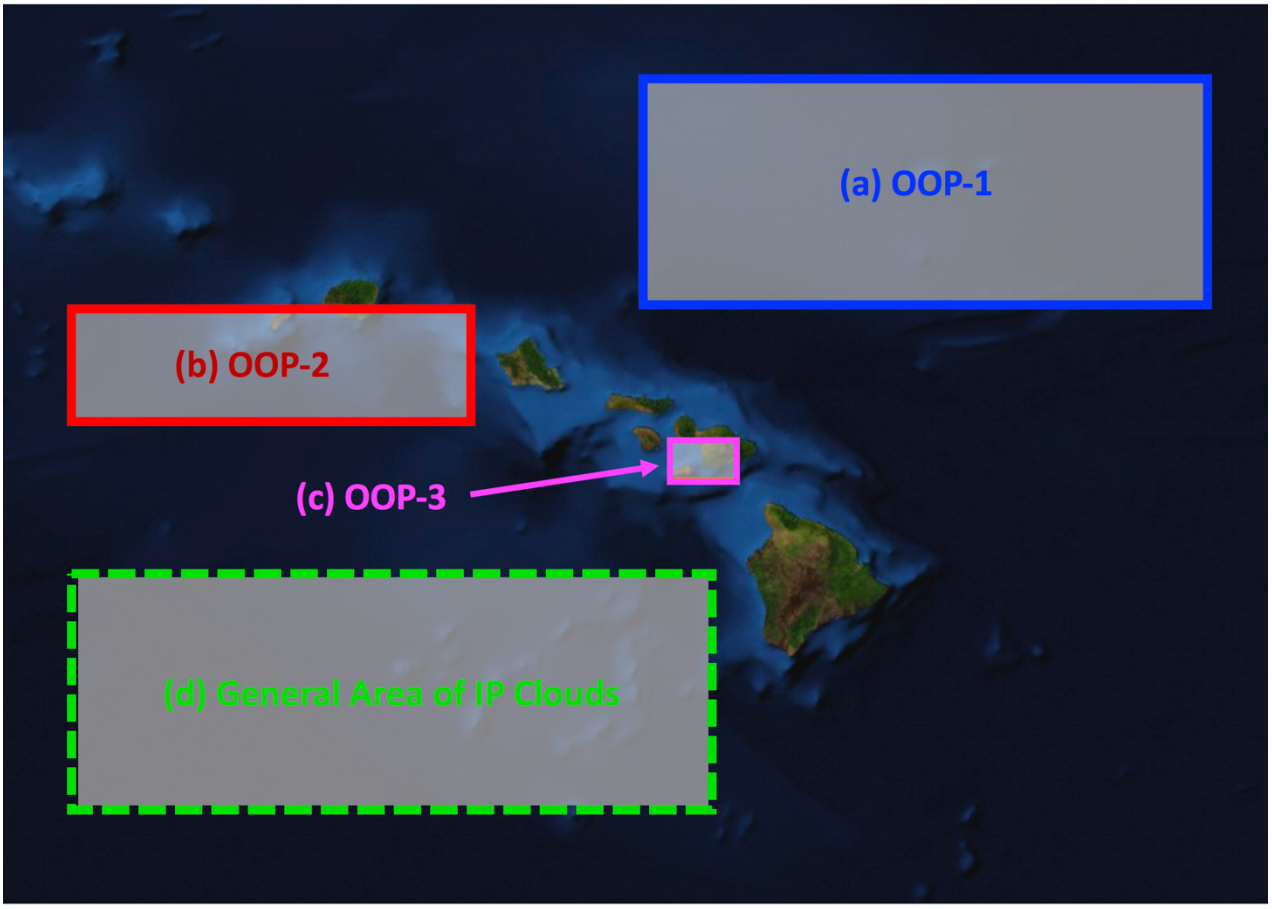

Figure 4.2. Map of the Hawaiian Islands illustrating the four major areas of interest in this study: (a) OOP-1, containing no orographic effects, (b) OOP-2, representing the cloud trails off Oahu and Kauai, (c) OOP-3, representing Maui's Makena cloud feature, and (d) the general area downwind of Kīlauea volcano in which IP clouds were observed.

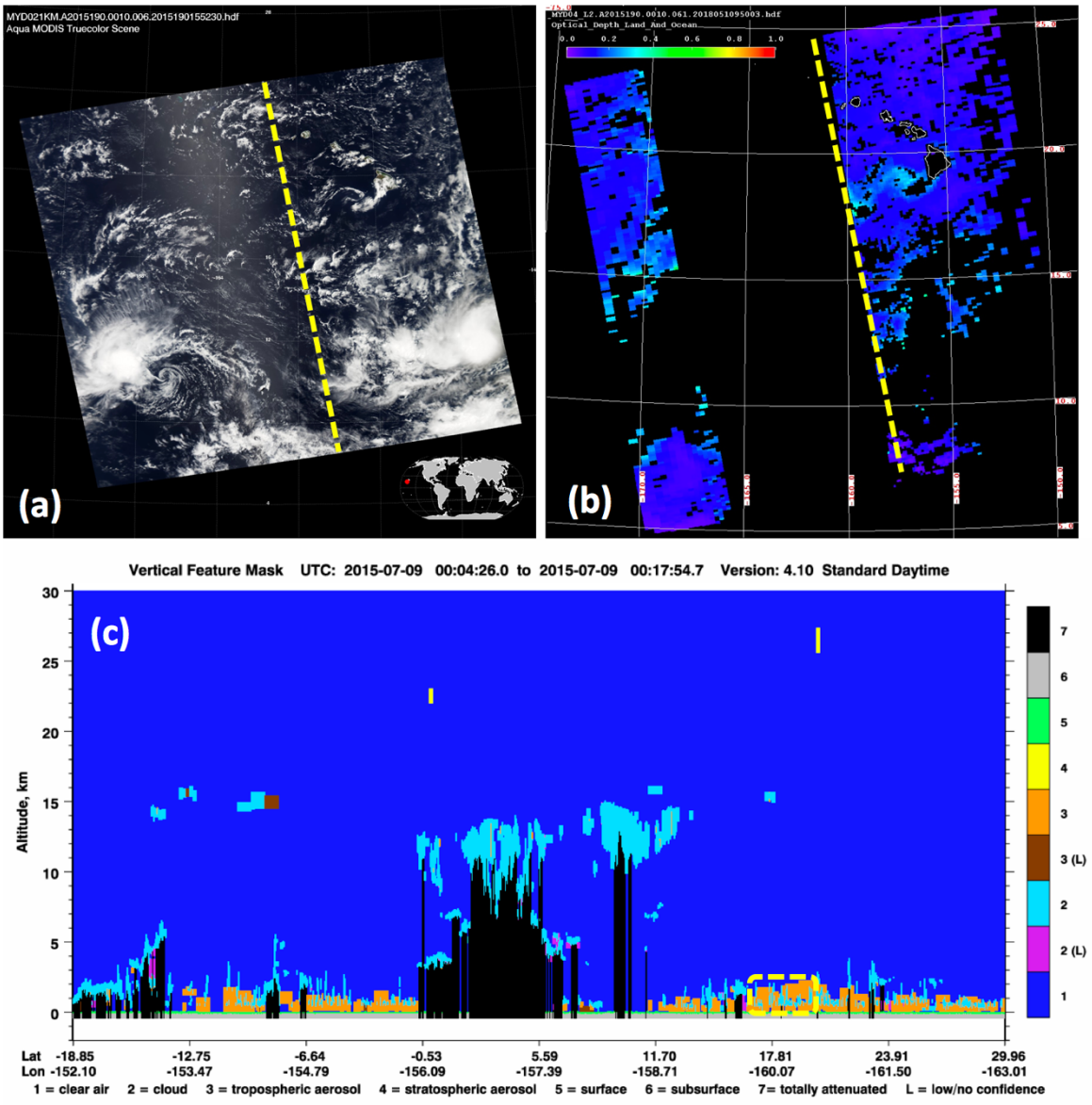

Figure 5.1. (a) MODIS/Aqua L1B visible image for 09 June 2015 at 0010Z and (b) MODIS/Aqua L2 AOD, in which the CALIOP/CALIPSO orbital track is marked (yellow dashed). (c) The corresponding VFM from CALIOP/CALIPSO from 00:04:26 UTC to 00:17:54.7 UTC, where the dashed yellow box centered near 17.81N, 160.07W shows tropospheric aerosol (orange) and clouds (light blue) interacting within the lowest 2.5 km.

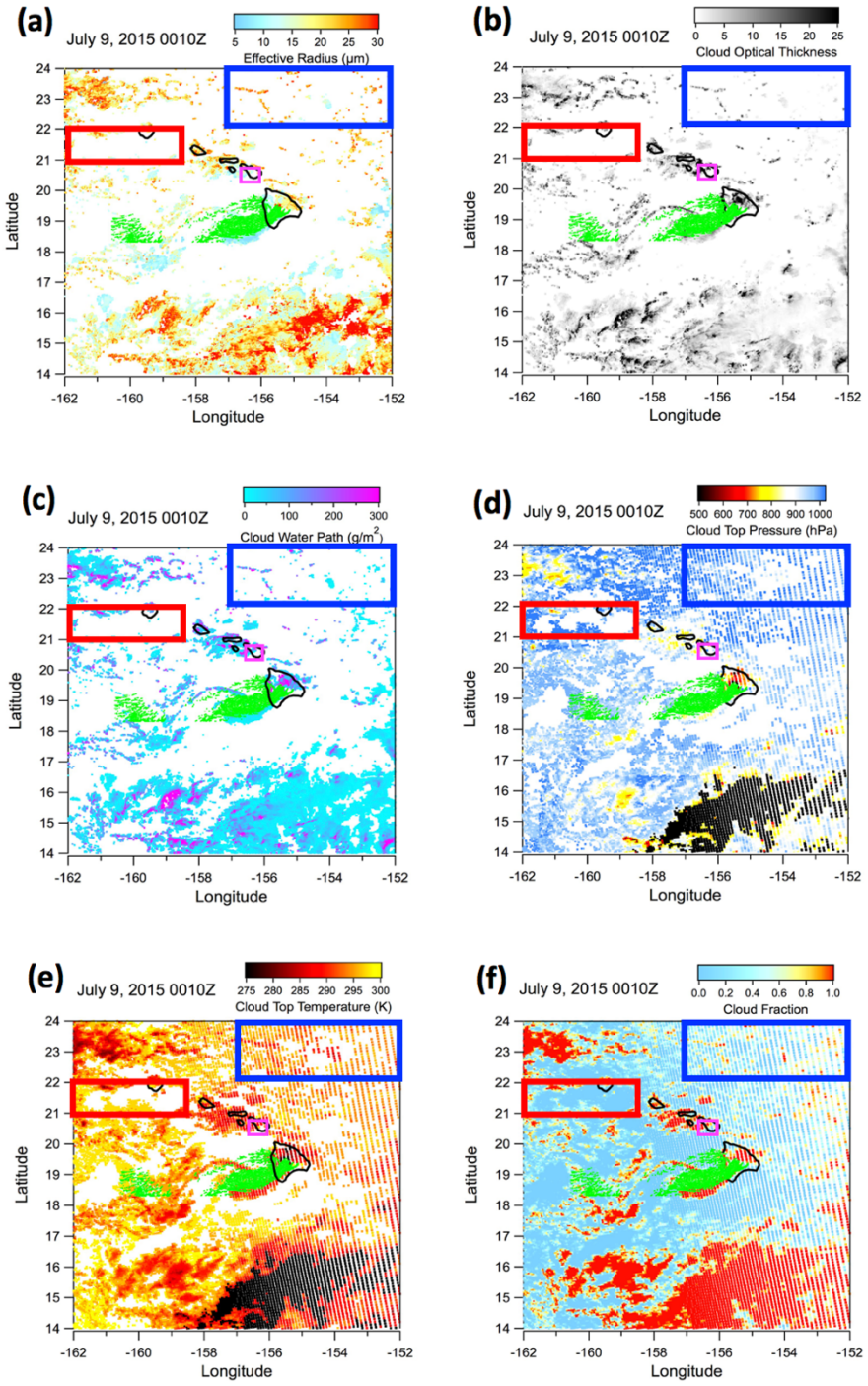

Figure 5.2. MODIS/Aqua L2 retrievals of (a) CER, (b) COT, and (c) CWP, at 1 km resolution, and (d) CTP, (e) CTT, and (f) CF, at a 5 km resolution for an illustrating case on 09 July 2015 at 0010Z. Areas of interest are shown: OOP-1 (in blue), OOP-2 (in red), OOP-3 (in magenta), and plume location from corresponding VMAP Vog model forecast (in green).

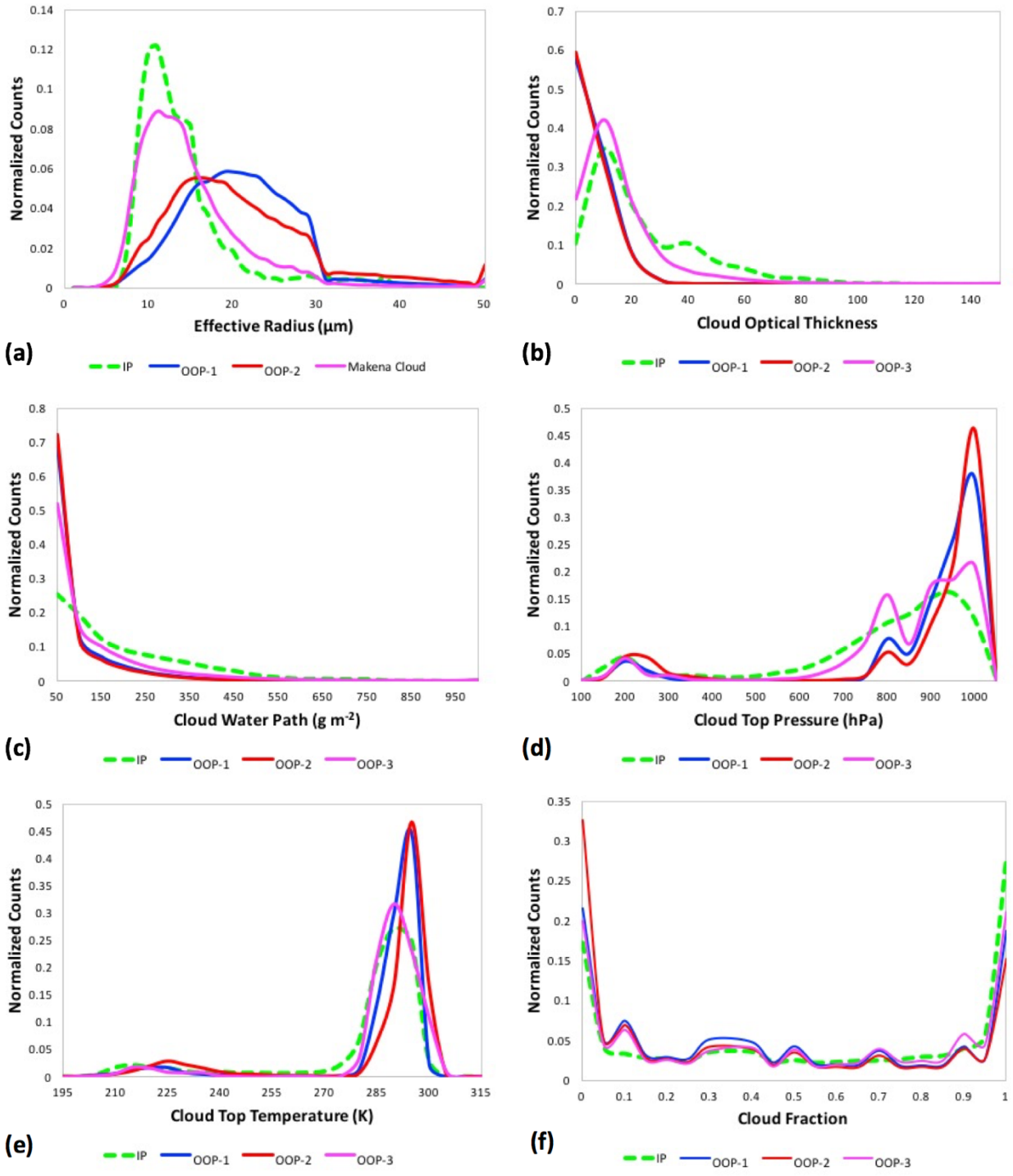

Figure 5.3. Overall results presented in relative histograms for MODIS L2 cloud properties: (a) CER, (b) COT, (c) CWP, (d) CTP, (e) CTT, and (f) CF, for IP and OOP (OOP-1, OOP-2, and OOP-3) clouds.

APPENDIX A

List of MODIS Cases

Using the data selection criteria overviewed in Section 4.1, we identified a total of 127 MODIS cases from JJA 2011 – 2017. The following is a list of the exact dates and times used in our study, where the date is followed by the Julian day in parenthesis and the hour-minute, HHMM, time stamp in coordinated universal time (UTC). Lastly, we include the hour of the corresponding VMAP Vog model forecast used for each case in brackets. Altogether, the appendix is organized by month and year, where the bolded number in parenthesis represents the number count of cases within each month. This information may be useful for future work.

June 2011 – (6)

June 8, 2011 (day 159) 2340	[23]
June 12, 2011 (day 163) 0010	[01]
June 15, 2011 (day166) 2345	[23]
June 21, 2011 (day 172) 0005	[01]
June 24, 2011 (day 175) 2340	[23]
June 28, 2011 (day 179) 0010	[01]

July 2011 – (5)

July 1, 2011 (day 182) 2345	[23]
July 10, 2011 (day 191) 2340	[23]
July 14, 2011 (day 195) 0010	[01]
July 17, 2011 (day 198) 2345	[23]
July 23, 2011 (day 204) 0005	[01]

August 2011 – (5)

August 2, 2011 (day 214) 2345	[23]
August 11, 2011 (day 223) 2340	[23]
August 18, 2011 (day 230) 2345	[23]
August 24, 2011 (day 236) 0005	[01]
August 27, 2011 (day 239) 2340	[23]

June 2012 – (6)

June 3, 2012 (day 155) 2335 [23]
June 7, 2012 (day 159) 0005 [01]
June 14, 2012 (day 166) 0010 [01]
June 23, 2012 (day 175) 0005 [01]
June 26, 2012 (day 178) 2340 [23]
June 30, 2012 (day 182) 0010 [01]

July 2012 – (6)

July 3, 2012 (day 185) 2345 [23]
July 9, 2012 (day 191) 0005 [01]
July 12, 2012 (day 194) 2340 [23]
July 19, 2012 (day 201) 2345 [23]
July 25, 2012 (day 207) 0005 [01]
July 28, 2012 (day 210) 2340 [23]

August 2012 – (7)

August 1, 2012 (day 214) 0010 [01]
August 6, 2012 (day 219) 2335 [23]
August 10, 2012 (day 223) 0005 [01]
August 13, 2012 (day 226) 2340 [23]
August 20, 2012 (day 233) 2345 [23]
August 22, 2012 (day 235) 2335 [23]
August 26, 2012 (day 239) 0005 [01]

June 2013 – (4)

June 13, 2013 (day 164) 2340 [23]
June 19, 2013 (day 170) 0000 [01]
June 26, 2013 (day 177) 0005 [01]
June 29, 2013 (day 180) 2340 [23]

July 2013 – (6)

July 12, 2013 (day 193) 0005 [01]
July 15, 2013 (day 196) 2340 [23]
July 19, 2013 (day 200) 0010 [01]
July 24, 2013 (day 205) 2335 [23]
July 28, 2013 (day 209) 0005 [01]
July 31, 2013 (day 212) 2340 [23]

August 2013 – (6)

August 4, 2013 (day 216) 0010 [01]

August 6, 2013 (day 218) 0000 [01]
August 13, 2013 (day 225) 0005 [01]
August 16, 2013 (day 228) 2340 [23]
August 25, 2013 (day 237) 2335 [23]
August 29, 2013 (day 241) 0005 [01]

June 2014 – (8)

June 6, 2014 (day 157) 0000 [01]
June 9, 2014 (day 160) 2335 [23]
June 13, 2014 (day 164) 0005 [01]
June 16, 2014 (day 167) 2340 [23]
June 20, 2014 (day 171) 0010 [01]
June 22, 2014 (day 173) 0000 [01]
June 25, 2014 (day 176) 2335 [23]
June 29, 2014 (day 180) 0005 [01]

July 2014 – (6)

July 2, 2014 (day 183) 2340 [23]
July 11, 2014 (day 192) 2335 [23]
July 18, 2014 (day 199) 2340 [23]
July 24, 2014 (day 205) 0000 [01]
July 25, 2014 (day 206) 2345 [23]
July 31, 2014 (day 212) 0005 [01]

August 2014 – (8)

August 3, 2014 (day 215) 2340 [23]
August 7, 2014 (day 219) 0010 [01]
August 12, 2014 (day 224) 2335 [23]
August 16, 2014 (day 228) 0005 [01]
August 19, 2014 (day 231) 2340 [23]
August 23, 2014 (day 235) 0010 [01]
August 26, 2014 (day 238) 2345 [23]
August 28, 2014 (day 240) 2335 [23]

June 2015 – (6)

June 3, 2015 (day 154) 2340 [23]
June 9, 2015 (day 160) 0000 [01]
June 16, 2015 (day 167) 0005 [01]
June 19, 2015 (day 170) 2340 [23]
June 25, 2015 (day 176) 0000 [01]
June 28, 2015 (day 179) 2335 [23]

July 2015 – (6)

July 2, 2015 (day 183) 0005 [01]
July 5, 2015 (day 186) 2340 [23]
July 9, 2015 (day 190) 0010 [01]
July 18, 2015 (day 199) 0005 [01]
July 25, 2015 (day 206) 0010 [01]
July 30, 2015 (day 211) 2335 [23]

August 2015 – (3)

August 10, 2015 (day 222) 0010 [01]
August 15, 2015 (day 227) 2335 [23]
August 29, 2015 (day 241) 2345 [23]

June 2016 – (6)

June 2, 2016 (day 154) 0005 [01]
June 14, 2016 (day 166) 2335 [23]
June 18, 2016 (day 170) 0005 [01]
June 21, 2016 (day 173) 2340 [23]
June 25, 2016 (day 177) 0010 [01]
June 28, 2016 (day 180) 2345 [23]

July 2016 – (6)

July 4, 2016 (day 186) 0005 [01]
July 7, 2016 (day 189) 2340 [23]
July 11, 2016 (day 193) 0010 [01]
July 14, 2016 (day 196) 2345 [23]
July 27, 2016 (day 209) 0010 [01]
July 30, 2016 (day 212) 2345 [23]

August 2016 – (3)

August 5, 2016 (day 218) 0005 [01]
August 12, 2016 (day 225) 0010 [01]
August 15, 2016 (day 228) 2345 [23]

June 2017 – (7)

June 1, 2017 (day 152) 2335 [23]
June 5, 2017 (day 156) 0005 [01]
June 8, 2017 (day 159) 2340 [23]
June 17, 2017 (day 168) 2335 [23]

June 21, 2017 (day 172) 0005 [01]
June 24, 2017 (day 175) 2340 [23]
June 28, 2017 (day 179) 0010 [01]

July 2017 – (7)

July 1, 2017 (day 182) 2345 [23]
July 7, 2017 (day 188) 0005 [01]
July 14, 2017 (day 195) 0010 [01]
July 17, 2017 (day 198) 2345 [23]
July 23, 2017 (day 204) 0005 [01]
July 26, 2017 (day 207) 2340 [23]
July 30, 2017 (day 211) 0010 [01]

August 2017 – (10)

August 2, 2017 (day 214) 2345 [23]
August 4, 2017 (day 216) 2335 [23]
August 8, 2017 (day 220) 0005 [01]
August 11, 2017 (day 223) 2340 [23]
August 15, 2017 (day 227) 0010 [01]
August 18, 2017 (day 230) 2345 [23]
August 20, 2017 (day 232) 2335 [23]
August 24, 2017 (day 236) 0005 [01]
August 27, 2017 (day 239) 2340 [23]
August 31, 2017 (day 243) 0010 [01]

REFERENCES

Ackerman, A. S., and O. B. Toon, 1996: Evaluation of the "Twomey effect" with numerical cloud models and comparisons with observations. *Nucleation and Atmospheric Aerosols 1996*, M. Kulmala and P. E. Wagner, Ed., Elsevier Sci. Inc., 788-791.

Ahrens C. D., 2012: Essentials of Meteorology: An Invitation to the Atmosphere, Sixth Edition. Belmont, CA, Brooks/Cole, Cengage Learning.

Albrecht, B. A., 1989: Aerosols, Cloud Microphysics, and Fractional Cloudiness. *Science*, **245**, 4923, doi:10.1126/science.245.4923.1227.

Beirle, S., C. Horman, M. Penning de Vries, S. Dorner, C. Kern, and T. Wagner, 2013: Estimating the volcanic emission rate and atmospheric lifetime of SO2 from space: A case study for Kīlauea volcano, Hawai'i. *Atmos. Chem. Phys. Discuss.*, **13**, 28 695–28 727, doi:10.5194/acpd-13-28695-2013.

Boucher, O., D. Randall, P. Artaxo, C. Bretherton, G. Feingold, P. Forster, V.-M. Kerminen, Y. Kondo, H. Liao, U. Lohmann, P. Rasch, S.K. Satheesh, S. Sherwood, B. Stevens and X.Y. Zhang, 2013: Clouds and Aerosols. In: Climate Change 2013: The Physical Science Basis. Contribution of Working Group I to the Fifth Assessment Report of the Intergovernmental Panel on Climate Change [Stocker, T.F., D. Qin, G.-K. Plattner, M. Tignor, S.K. Allen, J. Boschung, A. Nauels, Y. Xia, V. Bex and P.M. Midgley (eds.)]. Cambridge University Press, Cambridge, United Kingdom and New York, NY, USA.

Businger, S., R. Huff, A. Pattantyus, K. Horton, A. J. Sutton, T. Elias, and T. Cherubini, 2015: Observing and Forecasting Vog Dispersion from Kīlauea Volcano, Hawaii. *Bull. Amer. Meteor. Soc.*, **96**, 1667-1686. doi:10.1175/BAMS-D-14-00150.1.

Cao, G., T. W. Giambelluca, D. E. Stevens, and T. A. Schroeder, 2007: Inversion Variability in the Hawaiian Trade Wind Regime. *J. Climate*, **20**, 1145-1160, doi: 10.1175/JCLI4033.1.

Carlis, D. L., Y.-L. Chen, and V. R. Morris, 2010: Numerical Simulations of Island-Scale Airflow over Maui and the Maui Vortex under Summer Trade Wind Conditions. *Mon. Wea. Rev.*, **138**, 2706- 2736, doi:10.1175/2009MWR3236.1.

Casadevall, T. J., J. B. Stokes, L. Greenland, L. L. Malinconico, J. R. Casadevall, and B. T. Furukawa, 1987: SO_2 and CO_2 emission rates at Kīlauea Volcano, 1979-1984. *Volcanism in Hawaii*, Decker, R.W., T. L. Wright, and H. Stauffer, Eds., Geol. Surv. Prof. Pap. 1350, 771-780.

Cotton, W. R., G. Bryan, and S. C. van der Heever, 2010: Part II: The Dynamics of Clouds. *Storm and Cloud Dynamics: Second Edition.* Elsevier Science & Technology, Int. Geophys. Series vol. 99, pp. 809.

Derber, J. C., D. F. Parrish, and S. J. Lord, 1991: The new global operational analysis system at the National Meteorological Center. *Weather Forecasting*, **6**, 538-547.

Draxler, R. R., and G. D. Hess, 1997: Description of the HYSPLIT_4 modeling system. NOAA Tech. Memo. ERL ARL-224, NOAA Air Resources Laboratory, Silver Spring, MD, 24 pp.

Draxler, R. R., and G. D. Hess, 1998: An overview of the HYSPLIT_4 modeling system of trajectories, dispersion, and deposition. *Aust. Meteor. Mag.*, **47**, 295-308.

Draxler, R. R., 1999: HYSPLIT4 user's guide. NOAA Tech. Memo. ERL ARL-230, NOAA Air Resources Laboratory, Silver Spring, MD.

Ebmeier, S. K., A. M. Sayer, R. G. Grainger, T. A. Mather, and E. Carboni, 2014: Systematic satellite observations of the impact of aerosols from passive volcanic degassing on local cloud properties. *Atmos. Chem. Phys.*, **14**, 10601-10618. doi:10.5194/acp-14-10601-2014.

Eguchi, K., I. Uno, K. Yumimoto, T. Takemura, T. Y. Nakajima, M. Uematsu, and Z. Liu, 2011: Modulation of cloud droplets and radiation over the North Pacific by sulfate aerosol erupted from Mount Kīlauea. *SOLA*, **7**, 77-80, doi:10.2151/sola.2011-020.

Elias, T., A. J. Sutton, J. B. Stokes, and T. J. Casadevall, 1998: Sulfur dioxide emission rates of Kīlauea Volcano, Hawaii, 1979 – 1997. USGS Open-File Rep. 98-462, Version 1. [Available online at http://pubs.usgs.gov/of/1998/of98-462/.]

Elias, T., and A. J. Sutton, 2002: Sulfur dioxide emission rates from Kīlauea Volcano, Hawai‘i, an update: 1998 – 2001. USGS Open-File Rep. 02-460, 29 pp.

Elias, T., and A. J. Sutton, 2007: Sulfur dioxide emission rates from Kīlauea Volcano, Hawai‘i, an update: 2002 – 2006. USGS Open-File Rep. 2007-1114, Version 1.0, 37 pp.

Elias, T., and A. J. Sutton, 2012: Sulfur dioxide emission rates from Kīlauea Volcano, Hawai‘i, 2007–2010. USGS Open-File Rep. 2012–1107, 25 pp. [Available at http://pubs.usgs.gov/of/2012/1107/.]

Forster, P., V. Ramaswamy, P. Artaxo, T. Berntsen, R. Betts, D. W. Fahey, J. Haywood, J. Lean, D. C. Lowe, G. Myhre, J. Nganga, R. Prinn, G. Raga, M. Schulz, R. Van Dorland, 2007: Changes in atmospheric constituents and in radiative

forcing. Contribution of Working Group I to the Fourth Assessment Report of the Intergovernmental Panel on Climate Change. In: Solomon, S., D. Qin, M. R. Manning, Z. Chen, M. Marquis, K. B. Averyt, M. Tignor, H. L. Miller (eds.), *Climate Change 2007: The Physical Science Basis*. Cambridge University Press, Cambridge, United Kingdom / New York, NY, USA, pp. 131-217.

Gassó, S. 2008: Satellite observations of the impact of weak volcanic activity on marine clouds. *J. Geophys. Res.*, **113**, D14S19, doi:10.1029/2007JD009106.

Hartmann, D. L., and D. Doelling, 1980: On the net radiative effectiveness of clouds. *J. Geophys. Res.,* **96**, 869-891.

Hartmann, D. L., M. E. Ockert-Bell, and M. L. Michelsen, 1992: The effect of cloud type on Earth's energy balance: Global analysis. *J. Clim.*, **5**(11), 1281-1304.

Haywood, J. M., and O. Boucher, 2000: Estimates of the direct and indirect radiative forcing due to tropospheric aerosols: a review. *Rev. Geophys*., **38**, 513-543.

Hill, B., and E. Baum, 2001: Sulfur: Sulfur Emissions and Midwest Power Plants. Clean Air Task Force Rep.

Kaufman, Y. J., D. Tanre, and O. Boucher, 2002: A satellite view of aerosols in the climate system. *Nature,* **419**, 215-223, doi:10.1038/nature01091.

Klein, S. A., and D. L. Hartmann, 1993: The seasonal cycle of low stratiform clouds. *J. Climate*, **6**, 1587-1606.

Klein, S. A., D. L. Hartmann, J. R. Norris, 1995: On the relationships among low cloud structure, sea surface temperature, and atmospheric circulation in the summertime northeast Pacific. *J. Climate*, **8**, 1140-1155.

Kloesel, K. A., A 70-Year History of Marine Stratocumulus Cloud Field Experiments off the Coast of California. *Bull. Amer. Meteor. Soc.*, **73**, 1581-1585.

Kodama, K., and S. Businger, 1998: Weather and Forecasting Challenges in the Pacific Region of the National Weather Service. *Wea. And Forecasting*, **13**, 523-546.

Levy, R. C., S. Mattoo, L. A. Munchak, L. A. Remer, A. M. Sayer, F. Patadia, and N. C. Hsu, 2013: The Collection 6 MODIS aerosol products over land and ocean. *Atmos. Meas. Tech*., **6**, 2989-3034, doi:10.5194/amt-6-2989-2013.

Liu, J.-W., S.-P. Xie, and S.-P. Zhang, 2015: Effects of the Hawaiian Islands on the vertical structure of low-level clouds from CALIPSO lidar, *J. Geophys. Res. Atmos*., 120, 215–228, doi:10.1002/2014JD022410.

Lohmann, U., and J. Feichter, 2005: Global indirect aerosol effects: a review. *Atmos. Chem. Phys.,* **5**, 715-737. doi:10.5194/acp-5-715-2005.

Mace, G. G., and A. C. Abernathy, 2016: Observational evidence for aerosol invigoration in shallow cumulus downstream of Mount Kīlauea. *Geophys. Res. Lett.,* **43**, doi:10.1002/2016GL067830.

Meyer, A., D. Folini, U. Lohmann, and T. Peter, 2016: Tropical temperature and precipitation responses to large volcanic eruptions: Observations and AMIP5 simulations. *J. Climate*, **29**, 1325-1338, doi:10.1175/JCLI-D-15-0034.1.

McCormick, R., and J. H. Ludwig, 1967: Climate modification by atmospheric aerosols. *Science*, **156**, 1358-1359.

Myhre, G., D. Shindell, F.-M. Bréon, W. Collins, J. Fuglestvedt, J. Huang, D. Koch, J.-F. Lamarque, D. Lee, B. Mendoza, T. Nakajima, A. Robock, G. Stephens, T. Takemura and H. Zhang, 2013: Anthropogenic and Natural Radiative Forcing. In: Climate Change 2013: The Physical Science Basis. Contribution of Working Group I to the Fifth Assessment Report of the Intergovernmental Panel on Climate Change [Stocker, T.F., D. Qin, G.-K. Plattner, M. Tignor, S.K. Allen, J. Boschung, A. Nauels, Y. Xia, V. Bex and P.M. Midgley (eds.)]. Cambridge University Press, Cambridge, United Kingdom and New York, NY, USA.

Neiburger, M., D. S. Johnson, and C. –W. Chen, 1961: The Inversion over the Eastern North Pacific Ocean. In Studies of the Structure of the Atmosphere over the Eastern Pacific Ocean in Summer, vol. 1., University of Chicago Pressm 94 pp.

Norris, J. R., and A. Slingo, 2009: Trends in observed cloudiness and Earth's radiation budget: what do we not know and what do we need to know?. Clouds in the Perturbed Climate system: their relationship to energy balance, atmospheric dynamics, and precipitation, MIT Press, Cambridge, MA, USA.

Oppenheimer, C., B. Scaillet, R. S. Martin, 2011: Sulfur degassing from volcanoes; source conditions, surveillance, plume chemistry and Earth system impacts. *Rev. Mineral. Geochem.*, **73**, 363-421, doi:10.2138/rmg.2011.73.13.

Pattantyus, A. K., S. Businger, and S. G. Howell, 2018: Review of sulfur dioxide to sulfate aerosol chemistry at Kilauea Volcano, Hawaii. *Atmospheric Environment*, **185**, 262-271, doi:10.1016/j.atmosenv.2018.04.055.

Pincus, R., and M. B. Baker, 1994: Effect of precipitation on the albedo susceptibility of clouds in the marine boundary layer. *Nature*, **372**, 250-252.

Porter, J. N., and Coauthors, 2002: Sun photometer and lidar measurements of the plume from the Hawaii Kīlauea Volcano Pu'u O'o vent: Aerosol flux and SO2 lifetime. *Geophys. Res. Lett.*, **29**, doi:10.1029 /2002GL014744.

Platnick, S., M. D. King, K. G. Meyer, G. Wind, N. Amarasinghe, B. Marchant, G. T. Arnold, Z. Zhang, P. A. Hubanks, B. Ridgway, and J. Riedi, 2015: *MODIS Cloud Optical Properties: User Guide for the Collection 6 Level-2 MOD06/MYD06 Product and Associated Level-3 Datasets*. Version 1.0, Goddard Space Flight Center, 141 pp. (available at https://modis-images.gsfc.nasa.gov/_docs/C6MOD06OPUserGuide.pdf).

Robock, A., 2000: Volcanic eruptions and climate. *Rev. Geophys.*, **38(2)**, 191-219, doi:10.1029/1998RG000054.

Rogers, R. R., and M. K. Yau, 1989: *A Short Course in Cloud Physics: Third Edition*. Pergamon Press, 293 pp.

Russell, L. M., J. H. Seinfeld, R. C. Flagan, R. J. Ferek, D. A. Hegg, P. V. Hobbs, W. Wobrock, A. I. Flossmann, C. D. O'Dowd, K. E. Nielsen, and P. A. Durkee, 1999: Aerosol dynamics in ship tracks. *J. Geophys. Res.*, **104**, D24, 31,077-31,095.

Sanderson, M., 1993: *Prevailing trade winds: climate and weather in Hawaii*. Honolulu: University of Hawaii Press, 126 pp.

Schroeder, Thomas. "Climate Controls." Prevailing Trade Winds: Weather and Climate in Hawai'i. Honolulu: University of Hawai'i Press, 1993.

Schubert, W. H., J. S. Wakefield, E. J. Steiner, and S. K. Cox, 1979: Marine stratocumulus convection. Part II: Horizontally homogeneous solutions. *J. Atmos. Sci.*, **36**, 1308-1324.

Smith, R. B., and V. Grubišić, 1993: Aerial Observations of Hawaii's Wake. *J. Atmos. Sci.*, **50**(22), 3728-3750.

Smith, D. M., B. B. Booth, N. J. Dunstone, R. Eade, L. Hermanson, G. S. Jones, A. A. Scaife, K. L. Sheen, and V. Thompson, 2016: Role of volcanic and anthropogenic aerosols in the recent global surface warming slowdown. *Nature Climate Change*, **6**, 936-940, doi:10.1038/NCLIMATE3058.

Stein, A. F., R. R. Draxler, G. D. Rolph, B. J. B. Stunder, M. D. Cohen, and F. Ngan, 2015: NOAA's HYSPLIT atmospheric transport and dispersion modeling system. *Bull. Amer. Meteor. Soc.*, **96**, 2059-2077. http://dx.doi.org/10.1175/BAMS-D-14-00110.1

Stevens, B., and G. Feingold, 2010: Untangling aerosol effects on clouds and precipitation in a buffered system. *Nature*, **461**, 607-613. doi:10.1038/nature08281.

Twomey, S., 1977: Influence of pollution on shortwave albedo of clouds, *J. Atmos. Sci.*, **34**(7), 1149-1152.

Ueyoshi, K., J. O. Roads, F. Fujioka, D. E. Stevens, 1996: Numerical Simulation of the Maui Vortex in the Trade Winds. *J. Meteor. Soc. Japan*, **74**, 723-744.

Werner, F., F. Ditas, H. Siebert, M. Simmel, B. Wehner, P. Pilewskie, T. Schmeissner, R. A. Shaw, S. Hartmann, H. Wex, G. C. Roberts, and M. Wenddisch, 2014: Twomey effect observed from collocated microphysical and remote sensing measurements over shallow cumulus, *J. Geophys. Res. Atmos.,* **119**, 1534-1545, doi:10.1002/2013JD020131.

Wood, R., 2012: Stratocumulus clouds. *Mon. Weather Rev.*, **140**(8), 2373-2423, doi:10.1175/MWR-D-11-00121.1.

Xie, S. P., W. T. Liu, Q. Y. Liu, and M. Nonaka, 2001: Far-reaching effects of the Hawaiian Islands on the Pacific Ocean-atmosphere system. *Science*, **292**, 2057-2060.

Yang, Y., Y.-L. Chen, 2008: Effects of Terrain Heights and Sizes on Island-Scale Circulations and Rainfall for the Island of Hawaii during HaRP. *Mon. Wea. Rev.*, **136**, 120-146, doi:10.1175/2007MWR1984.1.

Yang, Y., S. P. Xie, and J. Hafner, 2008: The Thermal Wake of Kauai Island: Satellite Observations and Numerical Simulations. *J. Climate*, **21**, 4568-4586, doi:10.1175/2008JCLI1895.1.

Yuan, T., L. A. Remer, and H. Yu, 2011: Microphysical, macrophysical and radiative signatures of volcanic aerosols in trade wind cumulus observed by the A-Train. *Atmos. Chem. Phys.*, **11**, 7119-7132. doi:10.5194/acp-11-7119-2011.